Astronomy & Astrophysics manuscript no. 3414 31st March 2003
(DOI: will be inserted by hand later)

On coronal structures and their variability in active stars: the case of Capella observed with Chandra/LETGS

C. Argiroffi[1], A. Maggio[2], and G. Peres[1]

[1] Dipartimento di Scienze Fisiche ed Astronomiche, Sezione di Astronomia, Università di Palermo, Piazza del Parlamento 1, 90134 Palermo, Italy
[2] INAF - Osservatorio Astronomico di Palermo, Piazza del Parlamento 1, 90134 Palermo, Italy

Received 13 December 2002 / Accepted 28 March 2003

Abstract In this paper we present a detailed analysis of two X-ray spectra of Capella, taken eleven months apart with the Low Energy Transmission Grating Spectrometer (LETGS) of the *Chandra Observatory*. We have studied variability of the coronal emission over different time scales, both in the whole X-ray band and in narrow temperature ranges identified by lines. The comparison of the two observations shows that the whole coronal emission of Capella in March 2000 was 3% higher than in February 2001; there also appears to be a tendency, albeit a marginal one, for the hottest lines to show the largest changes between the two observations. A detailed search for short-term variability (on time scales ranging from 10^2 to 10^4s) in the emission of individual lines shows that in all cases the emission is compatible with a constant source; the firm upper limits of 5% – 10% to the source variability on short time scales suggests that the intense X-ray emission is due to stable coronal structures and not to flaring activity. We have also determined the coronal thermal structure, as described with the emission measure distribution vs. temperature and with the help of plasma density, derived from the analysis of the O VII, Ne IX, Mg XI and Si XIII He-like ion triplets. The emission measure distribution, $em(T)$, and the element abundances, have been reconstructed with the Markov-Chain Monte Carlo method by Kashyap & Drake; the $em(T)$ presents a previously known sharp peak around $\log T = 6.8 - 6.9$, but we have also found evidence of a small amount of plasma at $T > 10^7$ K. With the help of the $em(T)$ and the density values we have estimated the pressure and volume of the emitting plasma at different temperatures, and we have derived information about the structure of individual loops and about the population of loops having different maximum temperatures. Our results indicate that loops with higher maximum temperature have higher pressure and smaller volume than lower temperature loops.

Key words. X-rays: stars – techniques: spectroscopic – stars: activity – stars: coronae – stars: individual: Capella

1. Introduction

It is known that many stars have X-ray coronal emission which is up to several orders of magnitude higher than the solar one. The knowledge of the solar corona is the starting point for studies of the stellar X-ray emission because of the high spatial resolution and high signal to noise ratio achievable in solar observations. Therefore it is assumed that also stellar coronal emission is produced by hot and optically thin plasma located in the outer atmospheres of the stars and confined in loop structures by magnetic field. However, when describing coronae which have emission up to 10^4 times the solar value, we should exercise some care because we need to scale the solar corona to match the observed emission, and there are different ways to do this, for instance assuming larger emitting volumes and/or higher densities. Therefore, a natural question is which are the differences and which the analogies between the structures characterizing the coronae of active stars and the solar one.

The high resolution X-ray spectra today available from *Chandra* and *XMM-Newton* observations allow us to improve our modeling of the structures present in active stellar coronae. With these spectra it is possible to evaluate fluxes of individual lines in the X-ray band, and hence to discriminate the emission from coronal regions at different temperatures, to reconstruct the emission measure distribution, $em(T)$, and to estimate element abundances. Moreover electron density N_e and temperature T of different coronal regions can be inferred using spectroscopic diagnostics based on line ratios, and starting from these parameters we can infer the pressure and volume of the emitting plasma. Finally, by combining all these results we can derive useful information about the coronal loop population.

In order to understand whether the coronal structures are steady or dynamic it is also crucial to test the presence of variability in the X-ray emission over different time scales. The

Send offprint requests to: C. Argiroffi, e-mail: argi@oapa.astropa.unipa.it

combined spectral and temporal resolutions in each observation allow us to perform variability studies on short time scales (minutes, hours) of the plasma in narrow temperature ranges by selecting and analyzing photon arrival times of individual emission lines. The advantage of this procedure is that we study the plasma in temperature ranges narrower than those explored with broad band analysis.

Finally, we can analyze long term variability (months, years), possibly linked to phenomena like stellar magnetic cycles, by comparing observations taken at different times.

In the light of the above considerations we have chosen to analyze the X-ray emission from Capella, because it is an active binary star whose spectra have high signal to noise ratio; furthermore its emission has never shown evident flares, and our observations confirm this behavior, with the additional bonus of allowing us to study its corona as largely composed of steady loops.

Capella is a close spectroscopic binary, at a distance of 12.93 pc, consisting of a G8 and a G1 giant stars, with masses of 2.7 $M_{\odot}$ and 2.6 $M_{\odot}$, and radii of 12 $R_{\odot}$ and 9 $R_{\odot}$, respectively. It is a member of the class of the long-period RS CVn binaries, having an orbital period of 104 days, not synchronous with the rotational period of the components, whose separation is 160 $R_{\odot}$. The rotational velocities of the two components are quite different, in fact the G1 star rotates at 36 km s^{-1}, much larger than the 3 km s^{-1} of the G8 star (Hummel et al. 1994).

Capella is a very bright X-ray source and for this reason it has been observed by every X-ray and EUV space-borne observatory. With the currently available instrumentation it is possible to separate the spectral contribution of each stellar component in the UV band, but not in the X-ray band. Linsky et al. (1998) have analyzed spectra taken in 1995 and in 1996 with the Goddard High-Resolution Spectrometer of the *Hubble Space Telescope* (*HST*), and, by deblending the profile of the Fe XXI line at 1354 Å (which forms at 10^7 K), they found similar contributions from the two stellar components. Johnson et al. (2002), instead, analyzing the same Fe XXI line in the spectrum taken in 1999 with the *HST*/Space Telescope Imaging Spectrograph, have found that the G8 star contribution is negligible compared to the rapidly rotating G1 star. Johnson et al. suggest that the coronal emission of the G8 star is variable over time scales of a few years. This evidence is compatible with the results found by Dupree et al. (1999) who have analyzed several spectra obtained with *EUVE* since 1992; they have found variations, over time scales of about one year, of the coronal emission and of the hot part of the emission measure distribution. However a puzzling question is posed by the results reported by Young et al. (2001): they have analyzed a spectrum obtained with the *Far Ultraviolet Spectroscopic Explorer* in 2000, and they have found that the Fe XVIII line at 974.85 Å, which forms at $T = 10^{6.8}$ K, mainly comes from the G8 component.

Several authors, based on data from *EUVE*, (Dupree et al. 1993; Schrijver et al. 1995; Dupree et al. 1999; Brickhouse et al. 2000) have reconstructed the emission measure distribution, showing that the corona of Capella is characterized by a continuous temperature distribution with a sharp peak at $\log T \sim 6.8$. Recent works (Brinkman et al. 2000; Canizares et al. 2000; Phillips et al. 2001; Ness et al. 2001; Mewe et al. 2001; Behar et al. 2001; Audard et al. 2001) report the results obtained from the analysis of the high resolution spectra of Capella gathered with *Chandra* and *XMM-Newton*. They have used individual line fluxes to perform density and temperature diagnostics, to infer some indication about the temperature distribution, and to derive some properties about the loop structures, but none of these works presents a detailed differential emission measure reconstruction.

In this paper we report the analysis of two X-ray spectra of Capella obtained with the LETGS of the *Chandra Observatory*. Our aim, as stated above, is to evaluate the emission measure distribution and to analyze the He-like ion triplets to infer some properties about the population of loops in the corona of Capella. We have also investigated in detail the presence of any short-term variability, checking the X-ray light curves of individual emission lines. Moreover we have compared the results found from the two spectra analyzed, to evaluate any variation occurred in one year.

In Sect. 2 we report the data processing and the methods used for the analysis. The results are shown in Sect. 3, while in Sect. 4 we discuss our results and report our conclusions in Sect. 5.

2. Observations and data analysis

The LETGS on the *Chandra* X-ray observatory is a diffraction grating spectrometer which provides spectra in the wavelength range 1 − 170 Å, with nominal resolution of 0.05 Å (FWHM) over the whole bandpass.

We have analyzed two observations of Capella obtained with the LETGS on March 8, 2000, and on February 14, 2001, retrieved from the *Chandra X-ray Center* public archive. The exposure times are respectively 33.9 ks and 26.9 ks. These observations are part of the on-going long-term calibration of the *Chandra* spectrometers and, among those available in the *Chandra* public archive, they have a similar and relatively long exposure time. This characteristic allows us to compare easily the results obtained from the analysis of the two spectra, and to study possible variations in the corona of Capella over time scales of about one year. Moreover, each observation is sufficiently long to allow us to study short-term variability on time scales from few minutes to few hours.

The data have been re-processed using the standard tools in the software package CIAO V2.1. The end products of this processing are positive and negative-order source spectra extracted from bow tie regions which ensure an almost constant fraction (90%-95%, depending on the wavelength) of source photons collected at each wavelength. Background spectra are also extracted from two regions above and below the source spectrum, each one having a constant area scaling factor of 5 with respect to the source region.

We have performed the analysis of the source spectra using the software package PINTofALE V1.0 developed by Kashyap & Drake (2000) while the variability analysis within each observation was performed with the Collura et al. (1987) method (Sect. 3.5). The spectral analysis consisted of the following steps: line identification and fitting, reconstruction of the emis-

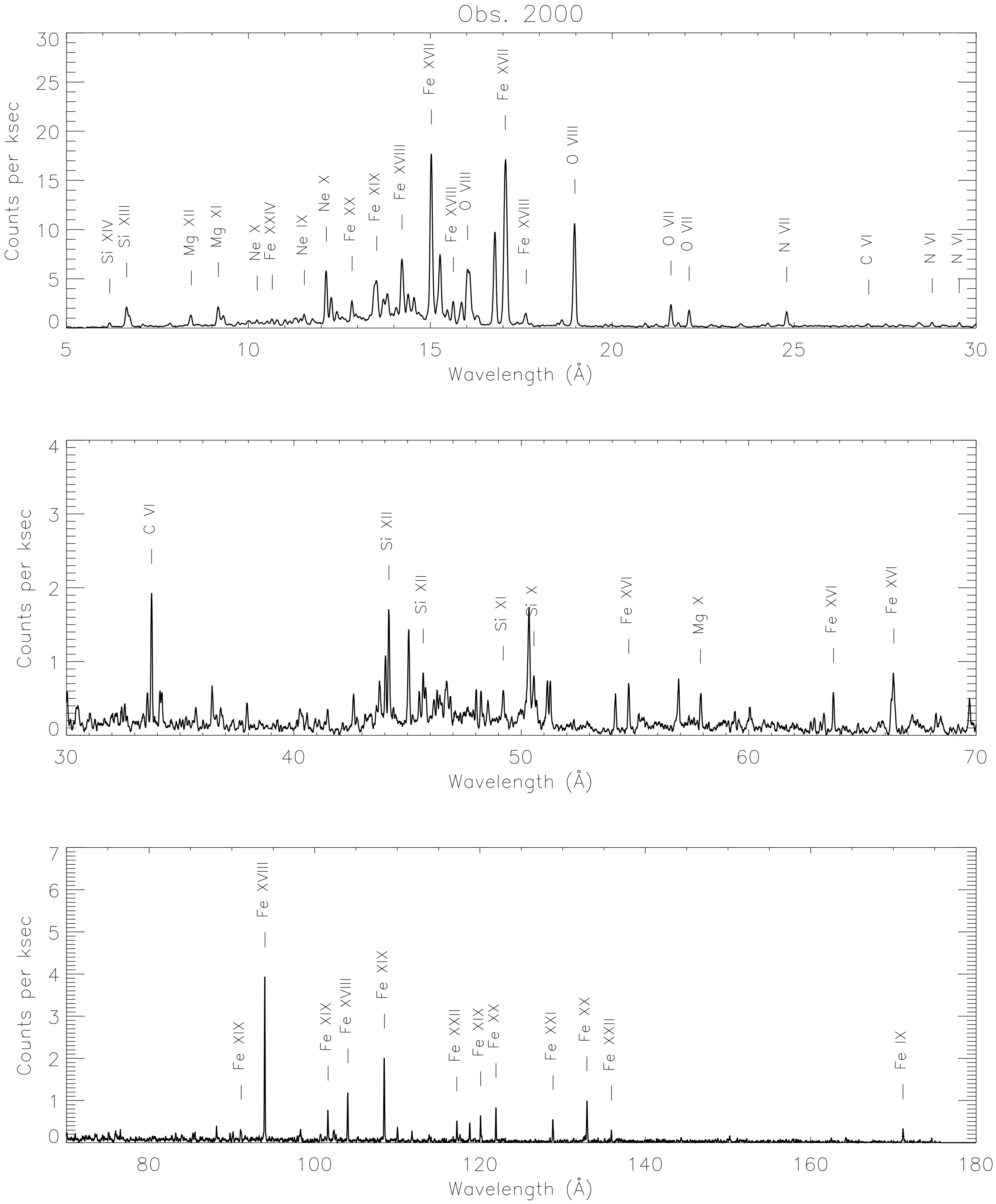

Figure 1. LETGS smoothed spectrum (positive and negative orders added) of Capella, with bin size of 0.0125 Å, collected on March 8, 2000, split into three parts. Note the different scales in each panel. The labels identify some of the strongest lines.

sion measure distribution with simultaneous determination of the element abundances, density and temperature diagnostics using He-like triplets. For the above analysis we have adopted the CHIANTI V3.03 emission line database, and the Mazzotta et al. (1998) ionization equilibrium.

In each spectrum we have identified and measured the fluxes of the strongest emission lines which are listed in Table 1. As an example, the spectrum of Capella observed in 2000 is shown in Fig. 1. The spectrum extracted from the 2001 observation is virtually identical.

Table 1. Strongest lines in the Capella spectrum.

			Identification				2000	2001	
Label	$\lambda^a_{\rm obs+}$	$\lambda^a_{\rm obs-}$	$\lambda^a_{\rm pred}$	Ion	Transition (*upper* → *lower*)	$\log T^b_{\rm max}$	$(F \pm \sigma)^c$	$(F \pm \sigma)^c$	$em(T)^d$
1a	6.19	6.19	6.18	Si XIV	$2p\ ^2P_{3/2} \rightarrow 1s\ ^2S_{1/2}$	7.20	105 ± 15	66 ± 13	AB
1b	···	···	6.19	Si XIV	$2p\ ^2P_{1/2} \rightarrow 1s\ ^2S_{1/2}$	7.20	···	···	
2	6.65	6.64	6.65	Si XIII	$1s\,2p\ ^1P_1 \rightarrow 1s^2\ ^1S_0$	7.00	417 ± 26	297 ± 23	AB
3	6.70	6.69	6.69	Si XIII	$1s\,2p\ ^3P_1 \rightarrow 1s^2\ ^1S_0$	6.95	99 ± 20	57 ± 18	
4	6.75	6.73	6.74	Si XIII	$1s\,2s\ ^3S_1 \rightarrow 1s^2\ ^1S_0$	7.00	202 ± 20	174 ± 19	
5a	8.43	8.40	8.42	Mg XII	$2p\ ^2P_{3/2} \rightarrow 1s\ ^2S_{1/2}$	7.00	297 ± 22	230 ± 20	AB
5b	···	···	8.42	Mg XII	$2p\ ^2P_{1/2} \rightarrow 1s\ ^2S_{1/2}$	7.00	···	···	
6	9.18	9.16	9.17	Mg XI	$1s\,2p\ ^1P_1 \rightarrow 1s^2\ ^1S_0$	6.80	446 ± 26	348 ± 24	AB
7	9.26	9.22	9.23	Mg XI	$1s\,2p\ ^3P_1 \rightarrow 1s^2\ ^1S_0$	6.80	110 ± 18	88 ± 16	
8	9.32	9.30	9.31	Mg XI	$1s\,2s\ ^3S_1 \rightarrow 1s^2\ ^1S_0$	6.80	236 ± 21	209 ± 19	
9a	10.24	10.23	10.24	Ne X	$3p\ ^2P_{3/2} \rightarrow 1s\ ^2S_{1/2}$	6.80	108 ± 18	96 ± 17	
9b	···	···	10.24	Ne X	$3p\ ^2P_{1/2} \rightarrow 1s\ ^2S_{1/2}$	6.80	···	···	
10a	10.66	10.65	10.62	Fe XXIV	$1s^2\,3p\ ^2P_{3/2} \rightarrow 1s^2\,2s\ ^2S_{1/2}$	7.30	126 ± 18	77 ± 16	AB
10b	···	···	10.66	Fe XXIV	$1s^2\,3p\ ^2P_{1/2} \rightarrow 1s^2\,2s\ ^2S_{1/2}$	7.30	···	···	
11a	11.02	11.00	10.98	Fe XXIII	$2s\,3p\ ^1P_1 \rightarrow 2s^2\ ^1S_0$	7.20	114 ± 18	75 ± 16	AB
11b	···	···	11.02	Fe XXIII	$2s\,3p\ ^3P_1 \rightarrow 2s^2\ ^1S_0$	7.20	···	···	
11c	···	···	11.02	Fe XVII	$2s\,2p^6\,4p\ ^1P_1 \rightarrow 2p^6\ ^1S_0$	6.80	···	···	
11d	···	···	11.03	Fe XXIV	$1s^2\,3d\ ^2D_{3/2} \rightarrow 1s^2\,2p\ ^2P_{1/2}$	7.30	···	···	
12	11.14	11.13	11.17	Fe XXIV	$1s^2\,3d\ ^2D_{5/2} \rightarrow 1s^2\,2p\ ^2P_{3/2}$	7.30	84 ± 17	60 ± 15	AB
13a	11.44	11.42	11.43	Fe XXIV	$1s^2\,3s\ ^2S_{1/2} \rightarrow 1s^2\,2p\ ^2P_{3/2}$	7.30	133 ± 19	102 ± 17	AB
13b	···	···	11.44	Fe XXII	$2s\,2p\,(^3P)\,3p\ ^2D_{3/2} \rightarrow 2s^2\,2p\ ^2P_{1/2}$	7.10	···	···	
14	11.54	11.53	11.55	Ne IX	$1s\,3p\ ^1P_1 \rightarrow 1s^2\ ^1S_0$	6.60	243 ± 22	176 ± 19	
15a	11.78	11.75	11.74	Fe XXIII	$2s\,3d\ ^1D_2 \rightarrow 2s\,2p\ ^1P_1$	7.20	149 ± 19	158 ± 19	AB
15b	···	···	11.77	Fe XXII	$2s^2\,(^1S)\,3d\ ^2D_{3/2} \rightarrow 2s^2\,2p\ ^2P_{1/2}$	7.10	···	···	
16a	12.14	12.13	12.12	Fe XVII	$2p^5\,4d\ ^1P_1 \rightarrow 2p^6\ ^1S_0$	6.80	1139 ± 40	899 ± 36	AB
16b	···	···	12.13	Ne X	$2p\ ^2P_{3/2} \rightarrow 1s\ ^2S_{1/2}$	6.80	···	···	
16c	···	···	12.14	Ne X	$2p\ ^2P_{1/2} \rightarrow 1s\ ^2S_{1/2}$	6.80	···	···	
17a	12.28	12.27	12.26	Fe XVII	$2p^5\,4d\ ^3D_1 \rightarrow 2p^6\ ^1S_0$	6.80	573 ± 31	349 ± 25	AB
17b	···	···	12.28	Fe XXI	$2s^2\,2p\,3d\ ^3D_1 \rightarrow 2p^2\ ^3P_0$	7.00	···	···	
18	12.44	12.42	12.44	Ni XIX	$2p^5\,3d\ ^1P_1 \rightarrow 2p^6\ ^1S_0$	6.90	275 ± 24	214 ± 21	AB
19a	12.85	12.84	12.82	Fe XX	$2s^2\,2p^2\,(^3P)\,3d\ ^4P_{3/2} \rightarrow 2s^2\,2p^3\ ^4S_{3/2}$	7.00	491 ± 29	338 ± 24	AB
19b	···	···	12.82	Fe XX	$2s^2\,2p^2\,(^3P)\,3d\ ^4P_{5/2} \rightarrow 2s^2\,2p^3\ ^4S_{3/2}$	7.00	···	···	
20a	13.46	13.45	13.45	Ne IX	$1s\,2p\ ^1P_1 \rightarrow 1s^2\ ^1S_0$	6.60	730 ± 35	619 ± 32	
20b	···	···	13.46	Fe XIX	$2p^3\,(^2D^*)\,3d\ ^3S_1 \rightarrow 2s^2\,2p^4\ ^3P_2$	6.90	···	···	
21	13.53	13.51	13.52	Fe XIX	$2p^3\,(^2D^*)\,3d\ ^3D_3 \rightarrow 2s^2\,2p^4\ ^3P_2$	6.90	723 ± 37	552 ± 33	AB
22a	13.57	13.55	13.55	Ne IX	$1s\,2p\ ^3P_1 \rightarrow 1s^2\ ^1S_0$	6.55	330 ± 30	265 ± 28	
22b	···	···	13.57	Fe XIX	$2p^3\,(^2D^*)\,3d\ ^3P_2 \rightarrow 2s^2\,2p^4\ ^3P_2$	6.90	···	···	
23	13.66	13.65	13.67	Fe XIX	$2p^3\,(^2D^*)\,3d\ ^3D_2 \rightarrow 2s^2\,2p^4\ ^3P_1$	6.90	143 ± 22	144 ± 21	A
24	13.71	13.70	13.70	Ne IX	$1s\,2s\ ^3S_1 \rightarrow 1s^2\ ^1S_0$	6.55	402 ± 30	306 ± 26	
25a	13.76	13.73	13.74	Fe XIX	$2p^3\,(^2D^*)\,3d\ ^1F_3 \rightarrow 2s^2\,2p^4\ ^1D_2$	6.90	178 ± 27	161 ± 24	
25b	···	···	13.74	Fe XX	$2s^2\,2p^2\,(^3P)\,3s\ ^4P_{5/2} \rightarrow 2s^2\,2p^3\ ^4S_{3/2}$	7.00	···	···	
26a	13.81	13.78	13.78	Ni XIX	$2p^5\,3s\ ^1P_1 \rightarrow 2p^6\ ^1S_0$	6.80	387 ± 31	244 ± 27	AB
26b	···	···	13.80	Fe XIX	$2p^3\,(^4S^*)\,3d\ ^3D_3 \rightarrow 2s^2\,2p^4\ ^3P_2$	6.90	···	···	
27	13.84	13.83	13.82	Fe XVII	$2s\,2p^6\,3p\ ^1P_1 \rightarrow 2p^6\ ^1S_0$	6.80	400 ± 31	257 ± 27	AB
28	13.90	13.86	13.89	Fe XVII	$2s\,2p^6\,3p\ ^3P_1 \rightarrow 2p^6\ ^1S_0$	6.75	134 ± 23	99 ± 20	
29a	13.96	13.94	13.95	Fe XX	$2s^2\,2p^2\,(^3P)\,3s\ ^4P_{1/2} \rightarrow 2s^2\,2p^3\ ^4S_{3/2}$	7.00	210 ± 22	133 ± 19	AB
29b	···	···	13.95	Fe XVIII	$2p^4\,(^1S)\,3d\ ^2D_{5/2} \rightarrow 2s^2\,2p^5\ ^2P_{3/2}$	6.90	···	···	
30	14.06	14.04	14.04	Ni XIX	$2p^5\,3s\ ^3P_1 \rightarrow 2p^6\ ^1S_0$	6.80	308 ± 25	258 ± 23	AB
31	14.10	14.10	14.08	Ni XIX	$2p^5\,3s\ ^3P_2 \rightarrow 2p^6\ ^1S_0$	6.80	195 ± 23	147 ± 20	AB
32a	14.22	14.20	14.20	Fe XVIII	$2p^4\,(^1D)\,3d\ ^2D_{5/2} \rightarrow 2s^2\,2p^5\ ^2P_{3/2}$	6.90	1318 ± 44	1044 ± 39	
32b	···	···	14.21	Fe XVIII	$2p^4\,(^1D)\,3d\ ^2P_{3/2} \rightarrow 2s^2\,2p^5\ ^2P_{3/2}$	6.90	···	···	
33	14.27	14.26	14.26	Fe XVIII	$2p^4\,(^1D)\,3d\ ^2S_{1/2} \rightarrow 2s^2\,2p^5\ ^2P_{3/2}$	6.90	528 ± 34	313 ± 28	AB

In order to perform the line fitting we have assumed, for the line profile, a beta-model of the form:

$$I(\lambda) = I_{\rm max} \frac{1}{\left[1 + \left(\frac{\lambda - \lambda_{\rm c}}{\Delta\lambda}\right)^2\right]^{\beta}} \qquad (1)$$

with the parameters $\Delta\lambda = 0.03$ Å and $\beta = 1.8$ kept fixed, while the values of $\lambda_{\rm c}$ and of the total line counts have been derived with the fitting procedure. The continuum has been approximated with a linear function in the proximity of each line; we

Table 1. Continued

Label	$\lambda^a_{\rm obs+}$	$\lambda^a_{\rm obs-}$	Identification $\lambda^a_{\rm pred}$	Ion	Transition (*upper* → *lower*)	$\log T^b_{\rm max}$	2000 $(F \pm \sigma)^c$	2001 $(F \pm \sigma)^c$	$em(T)^d$
34a	14.39	14.39	14.36	Fe XVIII	$2p^4\,(^1D)\,3d\,^2D_{3/2} \rightarrow 2s^2\,2p^5\,^2P_{1/2}$	6.90	667 ± 32	498 ± 28	AB
34b	···	···	14.37	Fe XVIII	$2p^4\,(^3P)\,3d\,^2D_{5/2} \rightarrow 2s^2\,2p^5\,^2P_{3/2}$	6.90	···	···	
35a	14.56	14.56	14.53	Fe XVIII	$2p^4\,(^3P)\,3d\,^2F_{5/2} \rightarrow 2s^2\,2p^5\,^2P_{3/2}$	6.90	629 ± 31	450 ± 27	AB
35b	···	···	14.55	Fe XVIII	$2p^4\,(^3P)\,3d\,^4P_{3/2} \rightarrow 2s^2\,2p^5\,^2P_{3/2}$	6.90	···	···	
36	15.03	15.02	15.02	Fe XVII	$2p^5\,3d\,^1P_1 \rightarrow 2p^6\,^1S_0$	6.75	3892 ± 65	3014 ± 59	AB
37a	15.20	15.19	15.18	O VIII	$4p\,^2P_{3/2} \rightarrow 1s\,^2S_{1/2}$	6.50	433 ± 30	389 ± 28	
37b	···	···	15.18	O VIII	$4p\,^2P_{1/2} \rightarrow 1s\,^2S_{1/2}$	6.50	···	···	
37c	···	···	15.20	Fe XIX	$2p^3\,(^4S^*)\,3s\,^5S_2 \rightarrow 2s^2\,2p^4\,^3P_2$	6.90	···	···	
38	15.28	15.27	15.26	Fe XVII	$2p^5\,3d\,^3D_1 \rightarrow 2p^6\,^1S_0$	6.75	1550 ± 45	1037 ± 39	AB
39	15.45	15.45	15.45	Fe XVII	$2p^5\,3d\,^3P_1 \rightarrow 2p^6\,^1S_0$	6.70	195 ± 23	169 ± 21	AB
40	15.48	15.51	15.50	Fe XVIII	$2s\,2p^5\,(^1P)\,3s\,^2P_{3/2} \rightarrow 2s\,2p^6\,^2S_{1/2}$	6.90	177 ± 22	112 ± 19	AB
41a	15.64	15.62	15.62	Fe XVIII	$2p^4\,(^1D)\,3s\,^2D_{5/2} \rightarrow 2s^2\,2p^5\,^2P_{3/2}$	6.90	518 ± 29	351 ± 25	
41b	···	···	15.63	Fe XX	$2s^2\,2p^2\,(^3P)\,3p\,^4S_{3/2} \rightarrow 2s\,2p^4\,^2S_{1/2}$	7.00	···	···	
42	15.84	15.82	15.83	Fe XVIII	$2p^4\,(^3P)\,3s\,^4P_{3/2} \rightarrow 2s^2\,2p^5\,^2P_{3/2}$	6.90	288 ± 26	271 ± 25	A
43	15.89	15.87	15.87	Fe XVIII	$2p^4\,(^1D)\,3s\,^2D_{3/2} \rightarrow 2s^2\,2p^5\,^2P_{1/2}$	6.80	336 ± 27	198 ± 24	
44a	16.02	16.00	16.00	Fe XVIII	$2p^4\,(^3P)\,3s\,^2P_{3/2} \rightarrow 2s^2\,2p^5\,^2P_{3/2}$	6.90	1092 ± 41	737 ± 35	
44b	···	···	16.01	O VIII	$3p\,^2P_{3/2} \rightarrow 1s\,^2S_{1/2}$	6.50	···	···	
44c	···	···	16.01	O VIII	$3p\,^2P_{1/2} \rightarrow 1s\,^2S_{1/2}$	6.50	···	···	
45	16.10	16.07	16.07	Fe XVIII	$2p^4\,(^3P)\,3s\,^4P_{5/2} \rightarrow 2s^2\,2p^5\,^2P_{3/2}$	6.90	1060 ± 41	820 ± 37	AB
46	16.18	16.16	16.17	Fe XVIII	$2s\,2p^5\,(^3P)\,3s\,^2P_{3/2} \rightarrow 2s\,2p^6\,^2S_{1/2}$	6.90	196 ± 23	151 ± 20	
47	16.27	16.25	16.31	Fe XVIII	$2s\,2p^5\,(^3P)\,3s\,^4P_{3/2} \rightarrow 2s\,2p^6\,^2S_{1/2}$	6.90	141 ± 21	78 ± 17	AB
48	16.33	16.31	16.34	Fe XVII	$2p^5\,3p\,^3D_2 \rightarrow 2p^6\,^1S_0$	6.70	156 ± 21	109 ± 18	
49	16.79	16.76	16.78	Fe XVII	$2p^5\,3s\,^3P_1 \rightarrow 2p^6\,^1S_0$	6.70	2190 ± 52	1654 ± 45	AB
50	17.06	17.03	17.05	Fe XVII	$2p^5\,3s\,^1P_1 \rightarrow 2p^6\,^1S_0$	6.70	2471 ± 62	1856 ± 56	AB
51	17.10	17.08	17.10	Fe XVII	$2p^5\,3s\,^3P_2 \rightarrow 2p^6\,^1S_0$	6.70	2357 ± 62	1674 ± 54	AB
52	17.64	17.61	17.64	Fe XVIII	$2p^4\,(^1D)\,3p\,^2P_{3/2} \rightarrow 2s\,2p^6\,^2S_{1/2}$	6.90	303 ± 23	252 ± 21	
53	18.63	18.61	18.63	O VII	$1s\,3p\,^1P_1 \rightarrow 1s^2\,^1S_0$	6.35	140 ± 18	118 ± 16	AB
54a	18.97	18.95	18.97	O VIII	$2p\,^2P_{3/2} \rightarrow 1s\,^2S_{1/2}$	6.50	2309 ± 53	1827 ± 47	AB
54b	···	···	18.97	O VIII	$2p\,^2P_{1/2} \rightarrow 1s\,^2S_{1/2}$	6.50	···	···	
55	21.61	21.61	21.60	O VII	$1s\,2p\,^1P_1 \rightarrow 1s^2\,^1S_0$	6.30	491 ± 27	413 ± 25	AB
56	21.82	21.81	21.81	O VII	$1s\,2p\,^3P_1 \rightarrow 1s^2\,^1S_0$	6.30	102 ± 15	88 ± 14	
57	22.11	22.11	22.10	O VII	$1s\,2s\,^3S_1 \rightarrow 1s^2\,^1S_0$	6.30	356 ± 23	313 ± 22	
58a	24.80	24.80	24.78	N VII	$2p\,^2P_{3/2} \rightarrow 1s\,^2S_{1/2}$	6.30	330 ± 23	234 ± 20	AB
58b	···	···	24.78	N VII	$2p\,^2P_{1/2} \rightarrow 1s\,^2S_{1/2}$	6.30	···	···	
59a	27.05	27.01	26.99	C VI	$4p\,^2P_{3/2} \rightarrow 1s\,^2S_{1/2}$	6.20	77 ± 14	54 ± 12	
59b	···	···	26.99	C VI	$4p\,^2P_{1/2} \rightarrow 1s\,^2S_{1/2}$	6.20	···	···	
60a	28.46	28.42	28.47	C VI	$3p\,^2P_{3/2} \rightarrow 1s\,^2S_{1/2}$	6.20	119 ± 16	74 ± 13	
60b	···	···	28.47	C VI	$3p\,^2P_{1/2} \rightarrow 1s\,^2S_{1/2}$	6.20	···	···	
61	28.80	28.78	28.79	N VI	$1s\,2p\,^1P_1 \rightarrow 1s^2\,^1S_0$	6.20	105 ± 15	91 ± 15	AB
62	29.54	29.53	29.53	N VI	$1s\,2s\,^3S_1 \rightarrow 1s^2\,^1S_0$	6.15	91 ± 15	59 ± 13	
63a	33.74	33.74	33.73	C VI	$2p\,^2P_{3/2} \rightarrow 1s\,^2S_{1/2}$	6.20	403 ± 25	286 ± 22	AB
63b	···	···	33.74	C VI	$2p\,^2P_{1/2} \rightarrow 1s\,^2S_{1/2}$	6.20	···	···	
64	44.03	44.03	44.02	Si XII	$1s^2\,3d\,^2D_{3/2} \rightarrow 1s^2\,2p\,^2P_{1/2}$	6.30	207 ± 20	174 ± 19	AB
65	44.18	44.18	44.17	Si XII	$1s^2\,3d\,^2D_{5/2} \rightarrow 1s^2\,2p\,^2P_{3/2}$	6.30	341 ± 23	276 ± 22	AB
66	45.51	45.52	45.52	Si XII	$1s^2\,3s\,^2S_{1/2} \rightarrow 1s^2\,2p\,^2P_{1/2}$	6.30	111 ± 16	63 ± 14	AB
67	45.69	45.68	45.69	Si XII	$1s^2\,3s\,^2S_{1/2} \rightarrow 1s^2\,2p\,^2P_{3/2}$	6.30	169 ± 18	149 ± 18	AB
68	49.21	49.21	49.22	Si XI	$2s\,3d\,^1D_2 \rightarrow 2s\,2p\,^1P_1$	6.20	115 ± 16	74 ± 14	AB
69a	50.56	50.55	50.52	Si X	$2s^2\,3d\,^2D_{3/2} \rightarrow 2s^2\,2p\,^2P_{1/2}$	6.20	152 ± 18	122 ± 16	AB
69b	···	···	50.57	Fe XVI	$4p\,^2P_{1/2} \rightarrow 3s\,^2S_{1/2}$	6.50	···	···	
70	50.68	50.66	50.69	Si X	$2s^2\,3d\,^2D_{5/2} \rightarrow 2s^2\,2p\,^2P_{3/2}$	6.20	75 ± 14	57 ± 13	AB
71	54.14	54.13	54.13	Fe XVI	$4d\,^2D_{3/2} \rightarrow 3p\,^2P_{1/2}$	6.50	112 ± 14	66 ± 11	AB
72	54.73	54.72	54.71	Fe XVI	$4d\,^2D_{5/2} \rightarrow 3p\,^2P_{3/2}$	6.50	154 ± 15	103 ± 14	AB

have checked the agreement between the predicted continuum level and the one used for line flux evaluation after reconstruction of the emission measure distribution, $em(T)$, and abundances computation. In case of line blends we have performed a multi-component fitting, and in all cases we have evaluated statistical uncertainties on λ_c and F at the 68% confidence level.

We have found the presence of small differences in the wavelength calibration between the positive and negative or-

Table 1. Continued

Label	$\lambda^a_{\rm obs+}$	$\lambda^a_{\rm obs-}$	Identification $\lambda^a_{\rm pred}$	Ion	Transition (*upper* → *lower*)	$\log T^b_{\rm max}$	2000 $(F \pm \sigma)^c$	2001 $(F \pm \sigma)^c$	$em(T)^d$
73	57.88	57.89	57.88	Mg X	$1s^2\,3p\ ^2P_{3/2} \rightarrow 1s^2\,2s\ ^2S_{1/2}$	6.10	99 ± 15	52 ± 13	AB
74	57.93	57.93	57.92	Mg X	$1s^2\,3p\ ^2P_{1/2} \rightarrow 1s^2\,2s\ ^2S_{1/2}$	6.10	38 ± 13	46 ± 13	AB
75	63.73	63.73	63.71	Fe XVI	$4s\ ^2S_{1/2} \rightarrow 3p\ ^2P_{3/2}$	6.45	121 ± 14	98 ± 13	
76	66.27	66.26	66.25	Fe XVI	$4f\ ^2F_{5/2} \rightarrow 3d\ ^2D_{3/2}$	6.50	86 ± 13	69 ± 12	AB
77	66.38	66.37	66.36	Fe XVI	$4f\ ^2F_{7/2} \rightarrow 3d\ ^2D_{5/2}$	6.50	125 ± 14	61 ± 12	AB
78	91.13	91.05	91.01	Fe XIX	$2s\,2p^5\ ^1P_1 \rightarrow 2s^2\,2p^4\ ^1D_2$	6.90	91 ± 14	69 ± 13	
79	94.00	93.96	93.92	Fe XVIII	$2s\,2p^6\ ^2S_{1/2} \rightarrow 2s^2\,2p^5\ ^2P_{3/2}$	6.80	979 ± 36	725 ± 32	
80	101.64	101.60	101.55	Fe XIX	$2s\,2p^5\ ^3P_1 \rightarrow 2s^2\,2p^4\ ^3P_2$	6.90	201 ± 19	139 ± 16	
81	104.04	103.99	103.94	Fe XVIII	$2s\,2p^6\ ^2S_{1/2} \rightarrow 2s^2\,2p^5\ ^2P_{1/2}$	6.80	319 ± 22	204 ± 19	
82	108.45	108.41	108.36	Fe XIX	$2s\,2p^5\ ^3P_2 \rightarrow 2s^2\,2p^4\ ^3P_2$	6.90	539 ± 28	326 ± 22	
83	117.21	117.21	117.18	Fe XXII	$1s^2\,2s\,2p^2\ ^2S_{1/2} \rightarrow 2s^2\,2p\ ^2P_{1/2}$	7.10	107 ± 15	83 ± 13	
84	118.79	118.77	118.68	Fe XX	$2s\,2p^4\ ^4P_{1/2} \rightarrow 2s^2\,2p^3\ ^4S_{3/2}$	7.00	100 ± 14	90 ± 14	
85	120.08	120.08	119.98	Fe XIX	$2s\,2p^5\ ^3P_2 \rightarrow 2s^2\,2p^4\ ^3P_1$	6.90	136 ± 16	97 ± 14	
86	121.95	121.93	121.84	Fe XX	$2s\,2p^4\ ^4P_{3/2} \rightarrow 2s^2\,2p^3\ ^4S_{3/2}$	7.00	191 ± 18	120 ± 15	
87	128.85	128.81	128.75	Fe XXI	$2s\,2p^3\ ^3D_1 \rightarrow 2p^2\ ^3P_0$	7.00	125 ± 15	78 ± 13	
88	132.94	132.92	132.84	Fe XX	$2s\,2p^4\ ^4P_{5/2} \rightarrow 2s^2\,2p^3\ ^4S_{3/2}$	7.00	141 ± 18	130 ± 17	
89	132.98	132.97	132.91	Fe XXIII	$2s\,2p\ ^1P_1 \rightarrow 2s^2\ ^1S_0$	7.10	150 ± 18	110 ± 16	
90	135.91	135.91	135.76	Fe XXII	$1s^2\,2s\,2p^2\ ^2D_{3/2} \rightarrow 2s^2\,2p\ ^2P_{1/2}$	7.10	55 ± 12	59 ± 12	
91	171.16	171.16	171.07	Fe IX	$3p^5\,3d\ ^1P_1 \rightarrow 3p^6\ ^1S_0$	5.80	74 ± 12	58 ± 10	AB

[a] Observed (for each order of the spectrum taken in 2000) and predicted (CHIANTI database) wavelengths in Å. In the cases of unresolved blends, identified by the same label number, we list the main components in order of increasing predicted wavelength.

[b] Temperature of maximum emissivity in K.

[c] Total line counts for each observation. In the cases of unresolved blends, identified by the same label number, we report only the total line counts.

[d] Lines selected to derive the emission measure distribution for the observation taken in 2000 (A) or 2001 (B).

der spectra, yielding relative differences in the line centroids of ≤ 0.04 Å, and also absolute differences with respect to the CHIANTI wavelengths up to 0.1 Å but only for lines with $\lambda \geq 90$ Å. In order to get over these calibration problems we have fitted separately the positive and negative spectra, and then we have summed the counts to obtain the total line counts. Given the high count rate of the source, this procedure causes only a small reduction of the signal to noise ratio on individual lines measurements.

3. Results

3.1. Line identification

We have identified Fe lines with ionization level ranging from Fe XVI up to Fe XXIV, plus the Fe IX line at 171 Å. We have also identified C, N, O, Ne, Mg, Si, and Ni lines. We have cross-checked our line list with those reported by Brinkman et al. (2000), Mewe et al. (2001), Phillips et al. (2001), Behar et al. (2001) and we have found overall consistency, with few exceptions possibly due to the different line databases adopted by us and by the other authors. In particular our identifications in the region between 10 and 12 Å are sometimes at variance from what reported by Phillips et al. (2001) and Behar et al. (2001): in fact we ascribe most of the spectral features observed to highly ionized iron lines (mainly Fe XXII-XXIV), supported by the recent experimental results reported by Brown et al. (2002) and by the line identifications reported by Ayres et al. (2001), while Phillips et al. and Behar et al. ascribe the same features to Fe XVII-XIX lines. Most of these lines are not included in the CHIANTI database because they originate from highly excited levels ($n \geq 4$). However we have verified that our results (Sect. 3.2) are not significantly affected by the lack of these lines in our analysis. More details about this issue are reported in Appendix A.

3.2. Emission measure distribution

Under the condition of optically-thin plasma the line photon flux relative to the transition of an ion between the levels $i \rightarrow f$, can be written as[1]:

$$F_{if} = \frac{1}{4\pi D^2} \int_T G_{if}(T, N_{\rm e})\ dem(T)\ {\rm d}\log T \quad (2)$$

where D is the star distance, $G_{if}(T, N_{\rm e})$ is the line contribution function and $dem(T)$ is the differential emission measure, defined as:

$$dem(T) = N_{\rm e}^2\ \frac{{\rm d}V(T)}{{\rm d}\log T} \quad (3)$$

[1] The exact relation between observed line counts and source emission measure contains three other factors due to instrumental effective area, exposure time and interstellar medium absorption. The first and the second are known, while for the latter we have assumed $N_H = 1.8 \times 10^{18}$ cm^{-2} (Linsky et al. 1993).

We have reconstructed the emission measure distribution from measured line fluxes using the Markov-Chain Monte Carlo (hereafter MCMC) method by Kashyap & Drake (1998), which allows us to estimate also the element abundances at the same time; this method has the additional advantage, over other procedures, of yielding uncertainties on the emission measure at various temperatures and on abundances[2].

The differential emission measure $dem(T)$ defined by Eq. 3 is a continuous function of temperature T; the MCMC method yields the volume emission measure distribution $em(T_n)$ defined over a pre-selected temperature grid; in our case the grid is characterized by $\Delta \log T = 0.1$ and ranges from $\log T = 5.7$ to $\log T = 7.5$. The final set of T_n over which the evaluation of uncertainties is possible depends on the temperatures of peak emissivity, $T_{\rm max}$, of the used lines: we can compute the $em(T_n)$ value, with its uncertainty, only if we have a sufficient number of lines with $T_{\rm max} \approx T_n$, i. e. enough information about the plasma emission at this temperature. In practice we are able to constrain the $em(T_n)$ between $\log T = 6.2$ and $\log T = 7.3$.

Before starting the MCMC procedure it is necessary to select a subset of the identified lines which is used to derive the emission measure distribution. We aimed at using only those lines that are most reliable, i. e. not blended, with sufficiently high signal to noise ratio and with flux compatible with that of other lines of the same element. Moreover we have eliminated density-sensitive lines otherwise the $em(T)$ derivation would be influenced by unrelated density effects; thanks to this choice the remaining lines have contribution functions which are only temperature dependent. It is worth noting that some subjectivity is introduced with the selection itself, but given the uncertainty of some of the atomic physics models and of some of the line measurements we must use only spectral information that we consider reliable.

In the last column of Table 1 we have indicated the lines selected for the $em(T_j)$ reconstruction. Note that we have excluded all the lines with $\lambda > 80$ Å, except the Fe IX line at 171 Å, because, for each iron ion, the emission measure distribution provided by short wavelength lines is significantly and consistently higher than that provided by long wavelength ones by a factor comprised between 2 and 5. We have decided to base our emission measure analysis on short wavelength lines because they are more numerous and cover a larger temperature range than the remaining long wavelength lines that we have excluded. In Appendix B we report a commented list of the selected lines.

Finally we emphasize that our identifications of the hot iron lines with $10\,\text{Å} < \lambda < 12\,\text{Å}$ (discussed in Sect. 3.1 and in Appendix A) are confirmed by the agreement between the emission measure provided by these lines and by other lines with similar $T_{\rm max}$.

The $em(T)$ distributions, derived for each observation, are shown in Fig. 2, where we have adopted $D = 12.93$ pc (Perryman et al. 1997). In order to check the quality of our result we have computed the line fluxes for all the identified lines in the spectrum and, in Fig. 3 we show the comparison between predicted and observed fluxes for the observation taken in 2000. The results obtained for the observation taken in 2001 are similar.

Figure 3 shows that for most lines there is agreement between predicted and observed fluxes within a factor 2, at $T = 10^{6.9}$ K there is a large spread due to Fe XVIII lines, while

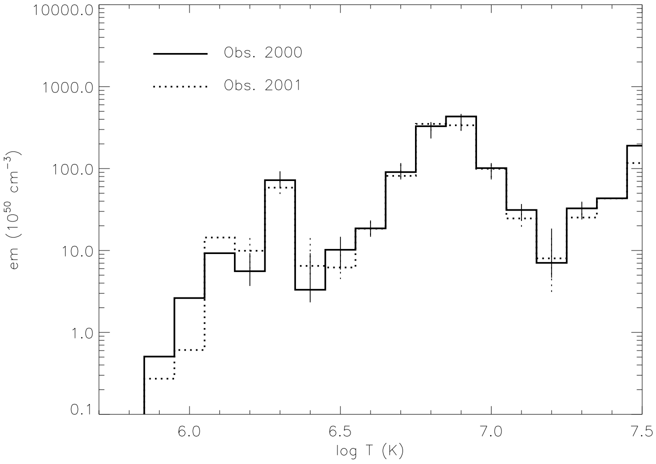

Figure 2. Emission measure distributions calculated with the MCMC method by Kashyap & Drake (1998) for the observation made on March 2000 (solid line) and for the observation made on February 2001 (dotted line). Note that we can provide error bars only for the bins ranging from $\log T = 6.2$ to $\log T = 7.3$.

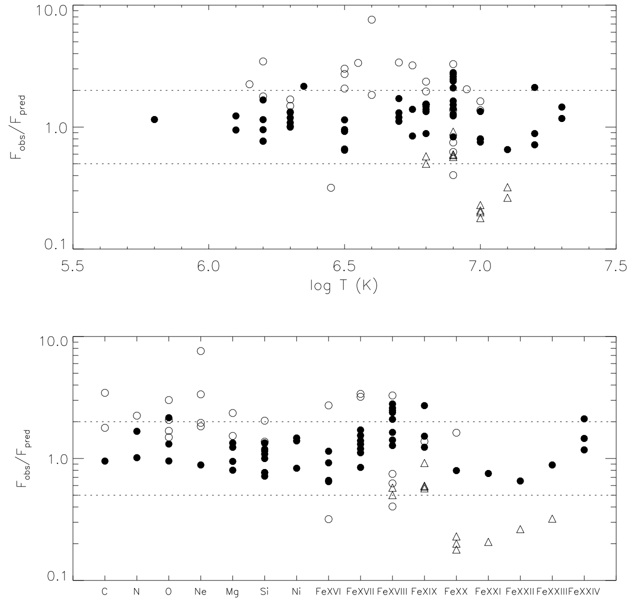

Figure 3. Comparison between observed and predicted line fluxes vs. $T_{\rm max}$ (upper panel) and vs. chemical elements and, for iron, ionization stage (lower panel). Filled symbols indicate the lines included in the emission measure reconstruction, open symbols indicate those not included, and triangles indicate the long wavelength lines ($\lambda > 80$ Å).

[2] As a matter of fact we can derive the product between the emission measure distribution and the iron abundance and we evaluate the abundance of the other elements as ratios with respect to the iron abundance.

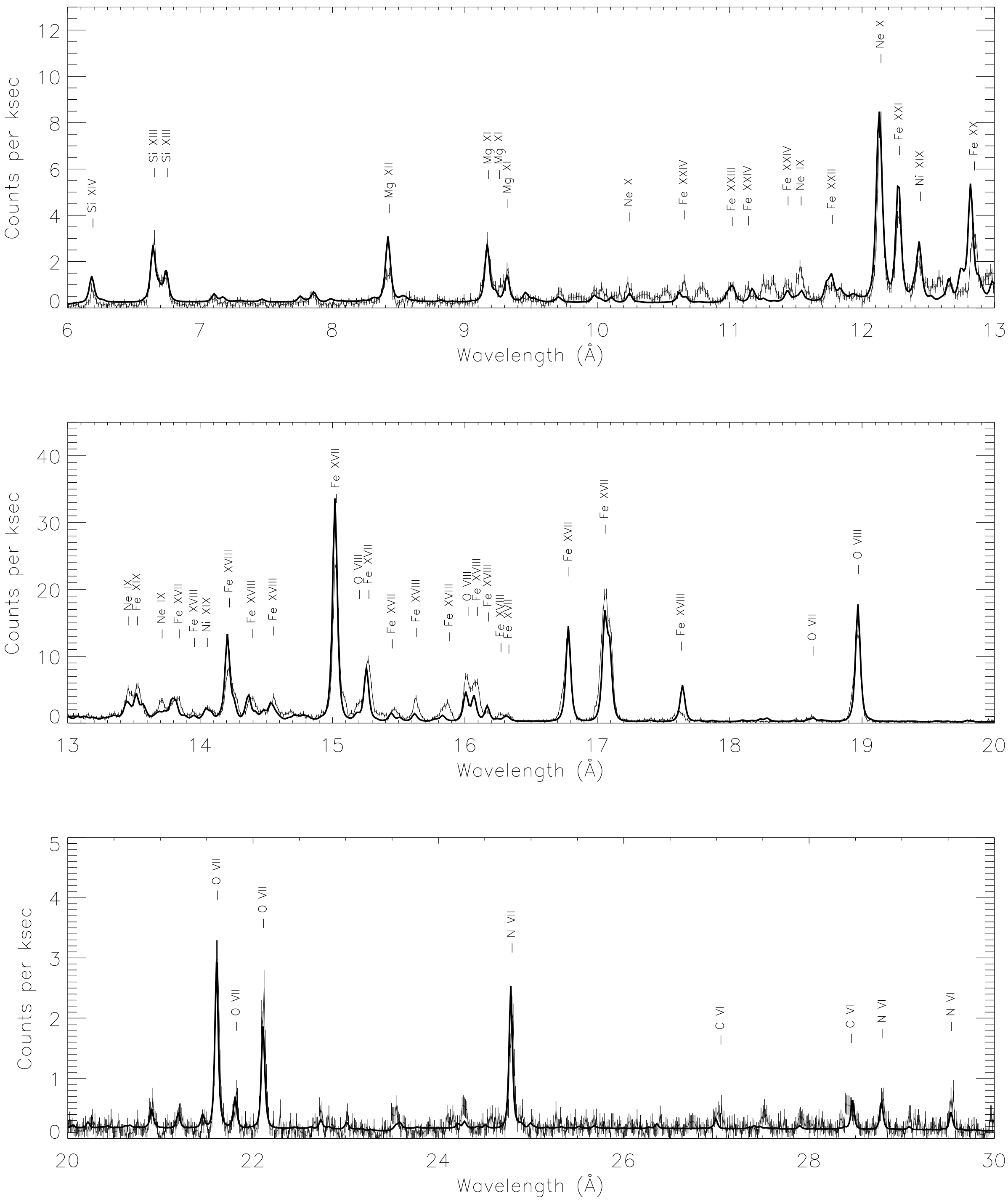

Figure 4. Comparisonn between LETGS spectrum of Capella (with error bars), collected on March 8, 2000, and the predicted spectrum (thick line) derived from the reconstructed emission measure distribution.

the long wavelength lines (triangles) have observed fluxes systematically lower than predicted, as already anticipated above. Finally, in Fig. 4 we compare the observed spectrum and the spectrum predicted on the basis of the $em(T)$ distribution we have derived, in the spectral region between 6 and 30 Å. The agreement is reasonably good, except in the region between 10 and 12 Å where the CHIANTI database does not contain the lines required to describe some of the observed spectral features (see Sect. 3.1 and Appendix A), and for some Fe XVIII lines affected by uncertainties in the CHIANTI database.

The $em(T)$ distributions that we have derived show a sharp peak near $\log T = 6.8 - 6.9$, in agreement with results obtained by Dupree et al. (1993), Schrijver et al. (1995) and Brickhouse et al. (2000), who derived the emission measure distribution

Table 2. Element abundances computed with the MCMC method.

		Obs. 2000		Obs. 2001	
	n^a	$N(X)/N(H)^b$	$N(X)/N(X)^c_\odot$	$N(X)/N(H)^b$	$N(X)/N(X)^c_\odot$
C	1	$(2.7^{+0.5}_{-0.7})\times10^{-4}$	$0.76^{+0.15}_{-0.18}$	$(2.5^{+0.7}_{-0.5})\times10^{-4}$	$0.71^{+0.20}_{-0.13}$
N	2	$(1.0^{+0.3}_{-0.2})\times10^{-4}$	$1.07^{+0.30}_{-0.20}$	$(1.02^{+0.27}_{-0.21})\times10^{-4}$	$1.10^{+0.29}_{-0.22}$
O	3	$(3.4^{+0.1}_{-0.8})\times10^{-4}$	$0.46^{+0.01}_{-0.11}$	$(3.7^{+0.4}_{-0.5})\times10^{-4}$	$0.50^{+0.05}_{-0.06}$
Ne	1	$(6.0^{+0.5}_{-0.8})\times10^{-5}$	$0.50^{+0.04}_{-0.07}$	$(6.0^{+0.4}_{-0.9})\times10^{-5}$	$0.50^{+0.03}_{-0.08}$
Mg	4	$(3.4^{+0.7}_{-0.8})\times10^{-5}$	$0.88^{+0.19}_{-0.21}$	$(3.6^{+0.5}_{-1.0})\times10^{-5}$	$0.94^{+0.14}_{-0.26}$
Si	9	$(3.1^{+1.0}_{-0.5})\times10^{-5}$	$0.87^{+0.28}_{-0.15}$	$(3.4^{+0.7}_{-0.8})\times10^{-5}$	$0.95^{+0.20}_{-0.22}$
Ni	3	$(2.6\pm0.6)\times10^{-6}$	1.5 ± 0.3	$(2.8^{+0.4}_{-0.8})\times10^{-6}$	$1.6^{+0.22}_{-0.5}$
Fe[d]	-	3.24×10^{-5}	1	3.24×10^{-5}	1

[a] Number of spectral lines of the relevant element included in the emission measure reconstruction.
[b] Element abundance relative to hydrogen.
[c] Element abundances relative to the solar ones (Grevesse et al. 1992).
[d] Coronal abundance equal to the solar value (Grevesse et al. 1992) as determined by adjustment of the continuum (see Sect. 3.3).

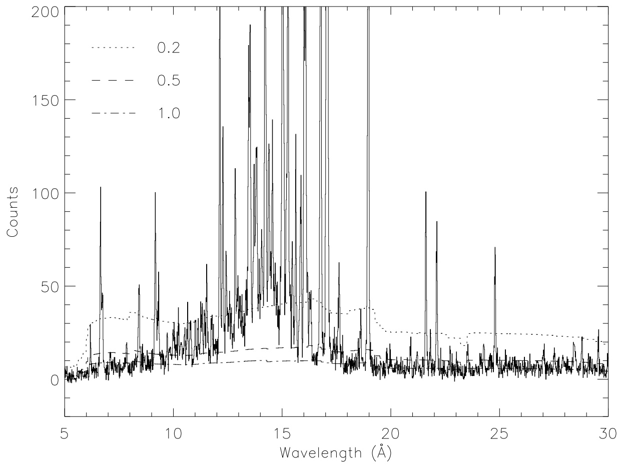

Figure 5. Comparison between observed spectrum (solid line) and predicted continuum spectra with different iron abundances (reported in the legend) relative to the Grevesse et al. (1992) solar value. Predicted continuum spectra are generated using the $em(T)$ and abundance values derived by the MCMC procedure, and $N_e = 10^{10}$ cm^{-3}. The best determination of the relative line to continuum ratio is achieved assuming a coronal metal abundance equal to the solar one.

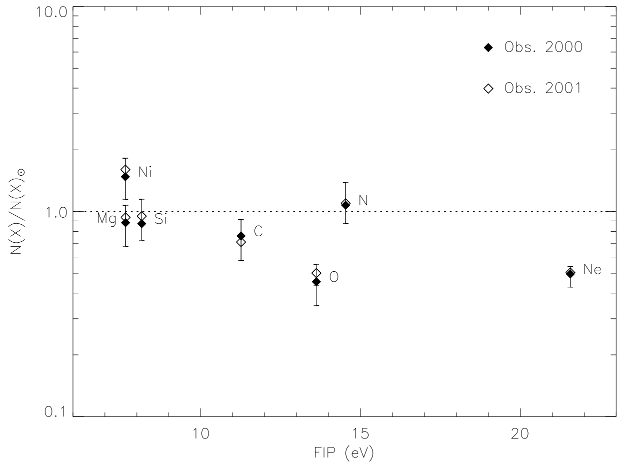

Figure 6. Derived abundances, in solar units (Grevesse et al. 1992), vs. first ionization potential. Filled diamonds are abundances derived from the observation taken on March 2000, open diamonds the ones derived from the observation taken on February 2001.

using *EUVE* data. A little amount of plasma is found at temperatures higher than 10^7 K (note however that the $em(T)$ at $\log T = 7.4 - 7.5$ is not constrained by error bars). These results suggest that the hot tail of emission measure distribution of Capella is larger than what found by Dupree et al. (1999) from an *EUVE* observation made in 1999.

By comparing the $em(T)$ obtained from the two spectra we can assert that the corona of Capella was approximately in the same $em(T)$ conditions after a period of 11 months.

We have derived the coronal global abundance of Capella by scaling the element abundances for various metallicities, and consequently the emission measure distribution, and then by comparing the observed spectrum with the predicted continuum level. To perform this check it is important to evaluate the continuum level without any influence of unresolved weak lines, therefore we have analyzed spectral regions which are free of emission lines according to the CHIANTI database. In Fig. 5 we show the predicted continuum spectra for different iron abundances relative to solar values superimposed to the observed one.

3.3. Metallicity and abundances

We have found that the coronal iron abundance of Capella is very similar to the solar photospheric value[3]. Bauer & Bregman (1996) have determined a global metal abundance of Capella of 0.2 times the solar one from a *ROSAT* observation. The disagreement observed in the global abundances between our value and the one by Bauer & Bregman may be related to the different resolutions of the studied spectra. Favata et al. (1997), analyzing data from *SAX*, have evaluated the value 0.98 ± 0.07,

[3] We use as reference value the Fe solar abundance reported by Grevesse et al. (1992), therefore we have converted metallicity reported by other authors to this one.

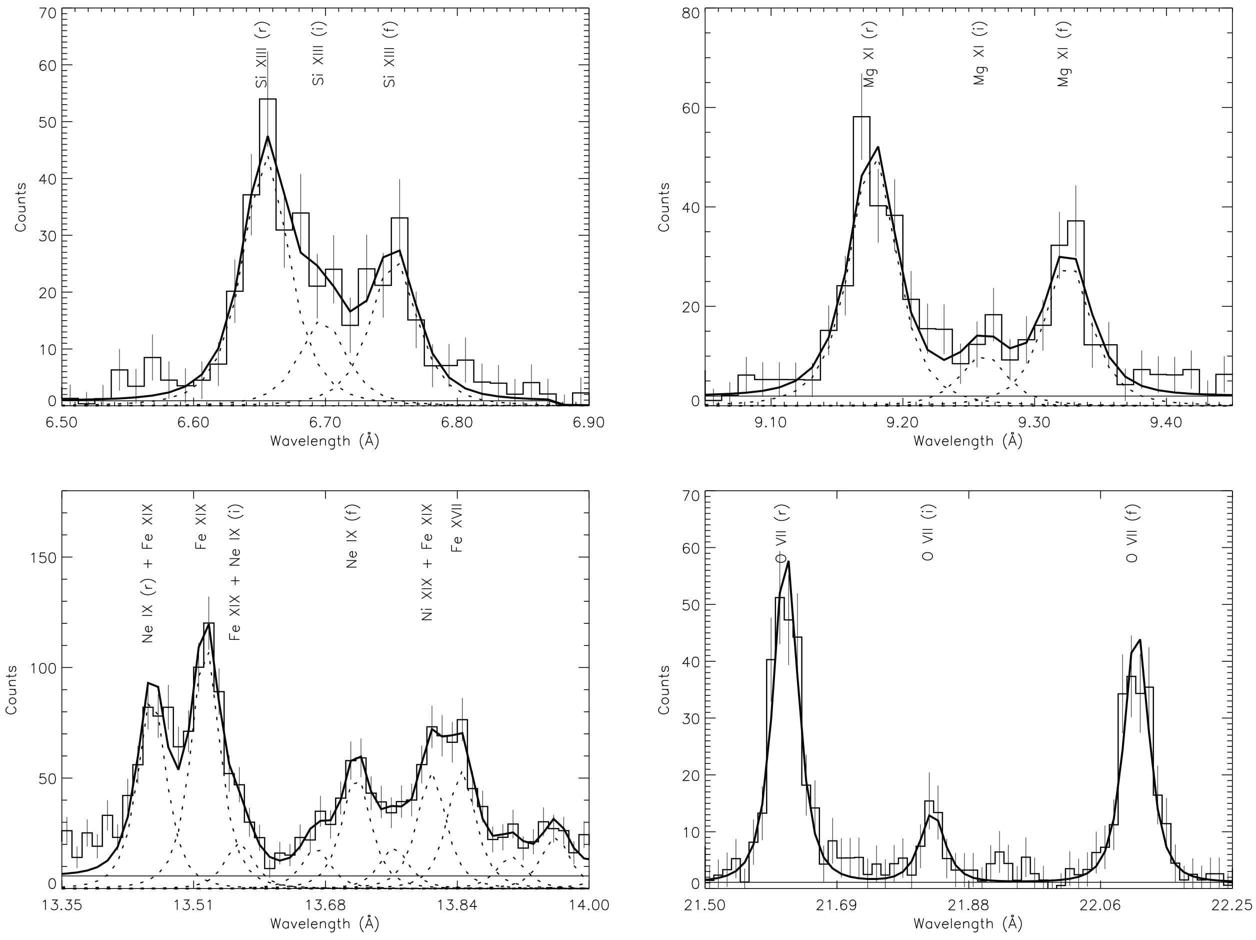

Figure 7. Observed and best-fit multi-component model spectrum for the Si xiii, Mg xi, Ne ix and O vii triplets of the positive order of the observation taken on March 2000. Dotted lines represent individual lines while the horizontal line indicates the continuum.

this result agrees with the values of 1.27 ± 0.19 and 1.04 ± 0.09 derived by Brickhouse et al. (2000) based on observations of *EUVE* and *ASCA* respectively and with the values of 0.90 ± 0.03 by Audard et al. (2001) obtained by analysis of the *XMM* RGS1 spectrum: all these findings are compatible with our determination. On the other hand the value 0.74 ± 0.01 derived by Audard et al. (2001) from the *XMM* RGS2 spectrum is rather small.

In Table 2 we report the element abundances obtained from each spectrum and the number of lines of each element included in the reconstruction of the emission measure distribution. In Fig. 6 we have plotted the derived abundances in solar units (Grevesse et al. 1992) versus the first ionization potential (FIP). We use the solar photospheric abundances as reference values because the Capella photospheric abundances are not known individually. The C, N, Mg, Si and Ni abundances are consistent (C and Ni within two standard deviations) with solar values, while O and Ne abundances are a factor 0.5 the solar ones.

Brickhouse et al. (2000) have found abundances of Ne, Mg, Si (from *ASCA* data), O and Ni (from *EUVE* data), compatible with our values, while the Si abundance derived from *EUVE* results larger by a factor 2. The abundances reported by Audard et al. (2001) agree with our results except for the case of Si and Ni for which the Audard et al. values are lower by a factor 2.

3.4. Density and temperature diagnostics from He-like ions

The relative intensity of the resonance, intercombination and forbidden lines (hereafter r, i, f) of the helium-like ions allows us to derive the plasma temperature, T, and electron density, N_e, averaged over the region in which the lines are formed (Gabriel & Jordan 1969; Porquet et al. 2001). In particular the density is determined by the ratio $R_D = f/i$, while the temperature by the ratio $R_T = (i + f)/r$.

The wavelength range of the LETGS includes the helium-like triplets of the ions C v, N vi, O vii, Ne ix, Mg xi and Si xiii, thus allowing to sample densities over the temperature range $10^6 - 10^7$ K. We have analyzed only the last four triplets, because the others are either too weak or affected by contamination by high-order spectra (see Ness et al. 2001, for the analysis of the C v and N vi triplets). The Mg xi and Si xiii triplets are partially blended, but it is possible to evaluate the fluxes of individual lines with a multi-component fitting. In Fig. 7 the observed and best-fit model spectra are shown.

Table 3. Density and temperature determination, from the line ratios $R_D = f/i$ and $R_T = (i+f)/r$, for the analysed He-like triplets

Obs. 2000					
Ion	R_D	N_e	R_T	$\log T$ (K)	$\log T_{max}(K)$
O VII	3.5 ± 0.6	$< 1 \times 10^{10}\ cm^{-3}$	0.95 ± 0.08	6.22 ± 0.08	6.3
Ne IX	3.2 ± 0.8	$< 2 \times 10^{11}\ cm^{-3}$	1.08 ± 0.10	6.21 ± 0.12	6.6
Mg XI	2.2 ± 0.4	$(2.0^{+2.0}_{-0.9}) \times 10^{12}\ cm^{-3}$	0.79 ± 0.08	6.64 ± 0.09	6.8
Si XIII	2.0 ± 0.5	$< 2.0 \times 10^{13}\ cm^{-3}$	0.73 ± 0.08	6.78 ± 0.11	7.0
Obs. 2001					
Ion	R_D	N_e	R_T	$\log T$ (K)	$\log T_{max}(K)$
O VII	3.6 ± 0.6	$< 1 \times 10^{10}\ cm^{-3}$	0.98 ± 0.09	6.18 ± 0.08	6.3
Ne IX	2.5 ± 0.6	$(1.8^{+2.5}_{-1.3}) \times 10^{11}\ cm^{-3}$	1.00 ± 0.10	6.29 ± 0.12	6.6
Mg XI	2.4 ± 0.5	$(1.5^{+1.7}_{-1.3}) \times 10^{12}\ cm^{-3}$	0.87 ± 0.09	6.54 ± 0.12	6.8
Si XIII	3.1 ± 1.0	$< 9 \times 10^{12}\ cm^{-3}$	0.78 ± 0.11	6.71 ± 0.14	7.0

The analysis of the Ne IX lines is especially difficult because of severe blending with Fe XIX lines (see the identifications from 20 to 29 in Table 1). It is worth noting that with the fitting procedure we are able to determine the total flux of each spectral feature, but not the flux of the unresolved line components which contribute to it. Therefore in order to perform the density and temperature diagnostics with the Ne IX triplet we need to derive the flux of the r and i Ne IX lines from the measured spectral features which include them. In the case of the resonance Ne IX line it is straightforward to use the emission measure distribution and the Ne/Fe abundance ratio to evaluate the relative intensities of the Ne IX and Fe XIX line components, and hence to derive the intensity of the r line of Ne IX from the measured total flux. Instead, in order to obtain the flux of the density-dependent intercombination line we have simply subtracted the predicted flux of the Fe XIX 13.57 Å line component from the measured total flux of the spectral feature # 22 of Table 1.

In Table 3 we report the R_D and R_T values for each ion and each spectrum, and the derived values of N_e and T. For all the triplets we have found a good consistency (within 1σ uncertainties) of the results obtained from the two spectra. Moreover, the values of the R_D and R_T ratios are compatible with those determined from the analysis of other Capella spectra obtained with *Chandra* or *XMM-Newton* (Brinkman et al. 2000; Canizares et al. 2000; Ness et al. 2001; Mewe et al. 2001; Phillips et al. 2001; Audard et al. 2001; Ness et al. 2002). Note however that, in some cases, the use of different models (Pradhan 1982, SPEX/MEKAL, Porquet & Dubau 2000 and Keenan et al. 1984) produces small differences for T (within a factor 2) and N_e (within a factor 5).

It is worth noting that all the temperatures we have found are lower than the corresponding temperatures of maximum line emissivity (T_{max}). This behavior will be commented in Sect. 4.

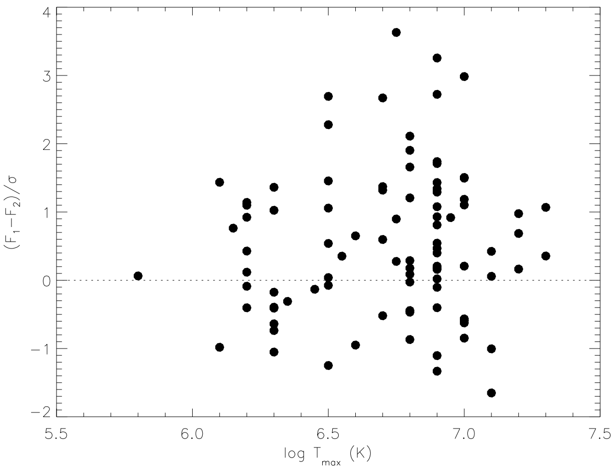

Figure 8. Comparison, in σ unit, between observed line fluxes of the two observations.

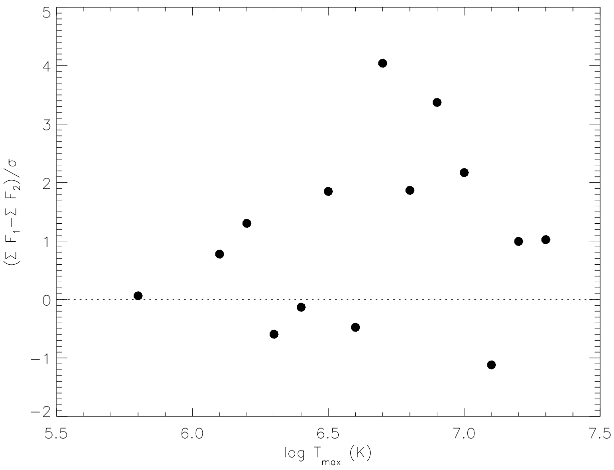

Figure 9. Comparison, in σ unit, between total observed line fluxes at each T_{max} of the two observations.

3.5. Variability

We have tested the presence of variability in the X-ray emission from Capella over different time scales and using different approaches: in order to look for variability on long-time scales we have compared the total count rates measured in the two observations, and we have compared the measured line counts of individual lines or groups of lines which form at similar T; moreover we have performed a detailed variability analysis on the light curves of individual emission lines, within each obser-

Table 4. Results for the short-term variability analysis. We report only upper limits for the effective variability at the 99.7% statistical level, because the emission is compatible with the hypothesis of constant source in the cases.

			Obs. 2000		Obs. 2001	
$\log T^{a}_{\max}$	$\Delta\lambda^{b}$	Ion	N^{c}_{TOT}	$V_{\rm eff}/I^{d}$ (%)	N^{c}_{TOT}	$V_{\rm eff}/I^{d}$ (%)
6.30	[21.50,22.25]	O VII	2557	< 10.3	2128	< 10.8
	[24.75,24.85]	N VII				
	[43.98,44.25]	Si XII				
	[45.58,45.75]	Si XII				
6.50	[15.95,16.05]	O VIII	3710	< 8.6	2797	< 9.4
	[18.85,19.05]	O VIII				
6.70	[14.95,15.12]	Fe XVII	13258	< 4.5	9966	< 5.0
	[15.22,15.33]	Fe XVII				
	[16.70,16.90]	Fe XVII				
	[16.95,17.20]	Fe XVII				
6.80	[9.05,9.45]	Mg XI	3891	< 8.4	2980	< 9.1
	[12.05,12.22]	Ne X				
	[93.90,94.10]	Fe XVIII				
	[103.93,104.12]	Fe XVIII				
6.90	[14.15,14.65]	Fe XVIII	8005	< 5.8	5841	< 6.5
	[15.55,15.70]	Fe XVIII				
	[15.80,15.93]	Fe XVIII				
	[16.05,16.20]	Fe XVIII				
	[17.58,17.66]	Fe XVIII				
	[101.55,101.70]	Fe XIX				
	[108.37,108.48]	Fe XIX				
7.00	[6.55,6.85]	Si XIII	3493	< 8.9	2465	< 10.0
	[8.30,8.50]	Mg XII				
	[12.22,12.35]	Fe XXI				
	[12.80,12.90]	Fe XX				
	[118.70,118.85]	Fe XX				
	[121.85,122.00]	Fe XX				
	[128.75,128.92]	Fe XXI				
	[132.85,133.05]	Fe XXIII				

[a] Peak temperature of line formation.
[b] Wavelength interval used to select photons. For each $T_{\max}$ value, we have analyzed together the photons extracted from all the listed wavelength intervals.
[c] Total number of selected photons, including the background.
[d] Effective fractional variability.

vation, with the aim to test for the presence of any short-term variability.

3.5.1. Variations over time scales of one year

A significant information can be derived from the mean source count rate relative to each observation: the computed values (2.726 ± 0.011 cts s^{-1} and 2.638 ± 0.012 cts s^{-1} for the 2000 and 2001 observations respectively) differ by 5 standard deviations and show that during the first observation the coronal emission was $\sim$3% more intense than one year later.

We have then compared the line intensities measured in the two spectra: Fig. 8 shows the differences between the line fluxes versus $T_{\max}$, the temperature of peak emissivity. All these differences are within 3σ, but it is evident that the fluxes of the first observation are systematically larger than those of the second, in agreement with the finding based on the mean count rate. Moreover the differences tend to be larger for the lines with formation temperatures between $10^{6.5}$ K and 10^{7} K. In order to improve the statistics we have summed all the fluxes from the lines with the same $T_{\max}$, and then we have compared the values obtained from the two observations (see Fig. 9); the maximum discrepancies are 4σ and 3.4σ for the groups of lines which forms at $\log T_{\max} = 6.7$ and 6.9 respectively. Note that at these temperatures, which are near the peak of the emission measure distribution, we have the higher values for the summed line fluxes, that is to say the best sensitivity to the variability of the line emission.

3.5.2. Short-term variability

We have performed a detailed search of short-term variability using the phase-averaged χ^2 method proposed by Collura et al. (1987). Following this procedure we have binned the photon arrival times in equal duration intervals, ranging from 50 s to 8000 s; then we have compared each binned light curve with a constant one. Since the χ^2 value depends on the bin size b and the initial phase φ, i. e. $\chi^2 = \chi^2\,(b, \varphi)$, according to Collura

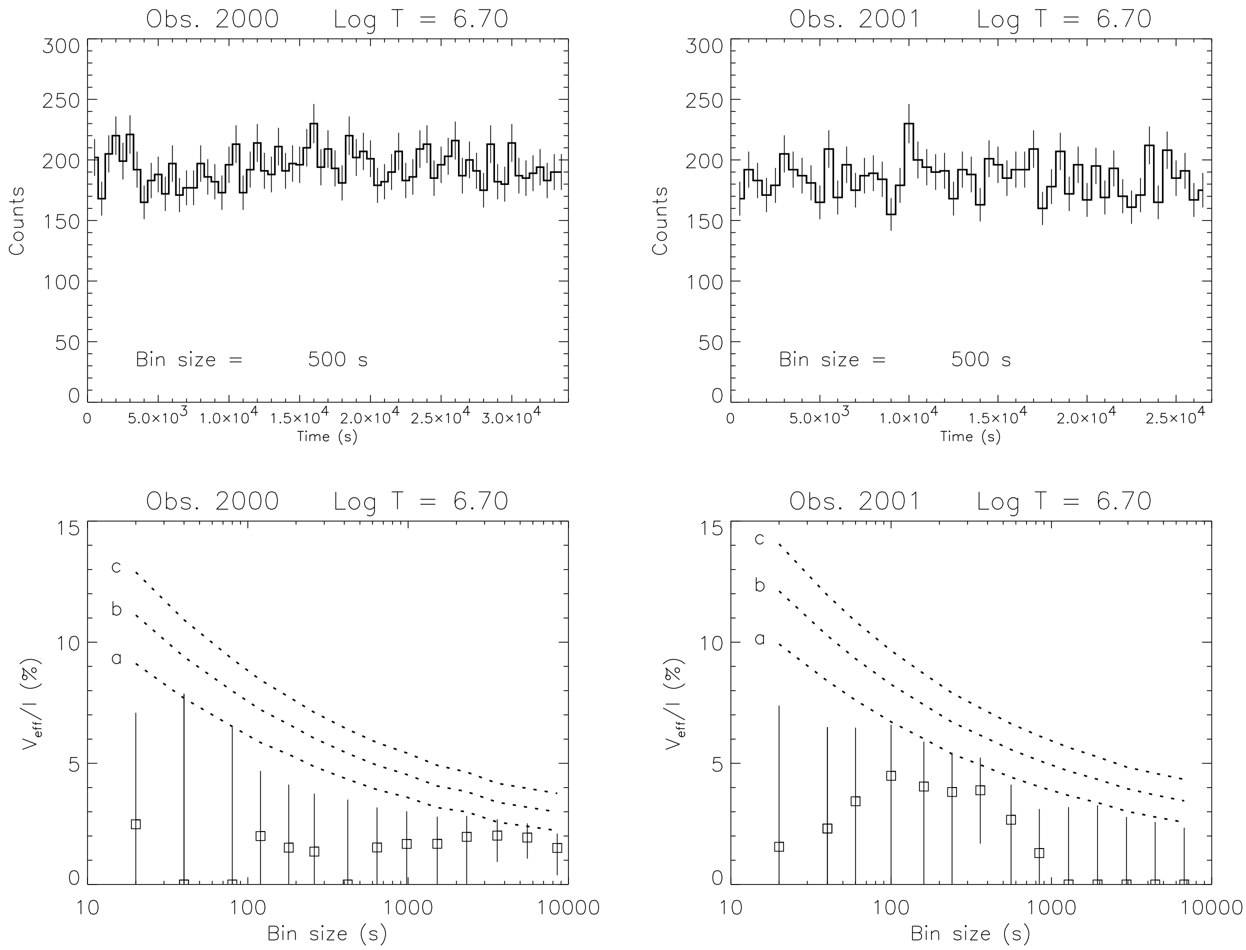

Figure 10. Light curves and effective variability for the lines at $T_{max} = 10^{6.7}$ K for both the observations. The upper panels show the light curves generated collecting all the photons of selected lines with the same T_{max} (see Table 4). The lower panels show the values of effective variability V_{eff}/I found for each bin size explored. Dotted curves correspond to the statistical confidence levels at (*a*) 95.45%, (*b*) 99.73% and (*c*) 99.99% that the null hypothesis of constant emission is true.

et al. we have evaluated for each bin size b the phase-averaged $\overline{\chi^2}(b)$ value, and then we have compared these values with statistical confidence levels computed under the hypothesis of a constant source. With this procedure it is possible to test, in a statistically significant way, the presence of variability, and then, assuming a pulsed variability model, to evaluate the characteristic time scale τ and the fractional variability level V_{eff}/I vs. the bin size b, where V_{eff} is the amplitude of the variable component and I is the average number of counts per bin (see Collura et al. 1987, for more details).

We have first applied this procedure to the arrival times of all the photons in each spectrum, finding that the emission is compatible with the hypothesis of a constant source, at high statistical confidence level. Note that the whole spectrum is the results of the emission by plasma characterized by a wide range of temperatures. In principle it is possible that the emission from small amounts of plasma, in narrow temperature ranges, may not be constant, and that this effect is lost analyzing the light curve of the whole spectrum. Therefore we have applied the method to individual lines, thus studying the variability of radiation emitted by the plasma with temperature close to T_{max} for each selected line.

For each line we have fixed a wavelength range $\Delta\lambda$ and we have extracted the photon arrival times in that range[4]. We have also analyzed together the arrival times of different lines with the same T_{max} value, in order to increase the photon counting statistics: in this way we were able to test for variability down to a sensitivity limit of 5-10%. In Fig. 10 we show the light curve and the plot of the effective variability vs. the bin size b for two representative cases. For each temperature, we have found that the emission is compatible with the hypothesis of a constant source. In Table 4 we report the results obtained including the effective variability upper limit at the 99.7% confidence level evaluated at a representative value of $b = 10^3$ s.

[4] It is worth noting that within each line spectral range it is not possible to distinguish the source emission in the spectral line from its continuum emission, and from the instrumental and sky background. This fact is not so important because, for all the lines we have considered, the contamination is a small fraction of the total number photons ($< 25\%$). Moreover we have verified that the background taken on both sides of the spectrum was constant.

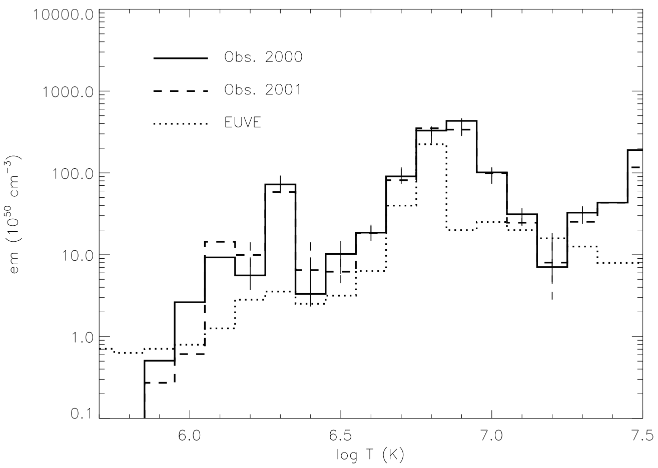

Figure 11. Our emission measure distributions (solid for observation taken in 2000 and dashed for observation taken in 2001) and EUVE emission measure distribution (dotted) obtained by Dupree et al. (2003).

4. Discussion

4.1. Variability

We have found a marginal long-term variability from the total count rate, but also by comparing line fluxes measured one year apart. Both these methods have shown that during the observation made in 2000 the coronal emission was 3% (at 5σ level) higher than during the second one made in 2001. On the other hand, we have found overall compatibility between the emission measure distributions of the two observations, given the higher error bars in $em(T)$. We have found that the largest differences between measured line counts occur for lines with $T_{\max}$ near the peak temperature of the emission measure distribution, which are also those with the highest signal to noise ratio.

The search of short-term variability inside each observation allows us to pose only upper limits on variable components, suggesting that the coronal structure of Capella is stable on time scales ranging from one minute to a few hours. It is reasonable to assume that the X-ray coronal emission is produced by relatively stable structures. This is consistent with the fact that Capella does not show large flux variations.

4.2. Emission measure distribution and coronal loop population

Figure 11 shows the $em(T)$ derived from the two *Chandra* observations together with the $em(T)$ derived from *EUVE* data by Dupree et al. (2003), based on an observation made in 2001. Our emission measure has a peak at $T_j = 10^{6.9}$ K wider than that found by Dupree et al.. Moreover, we observe a large difference at $T_j = 10^{6.3}$ K between our $em(T_j)$ and the one from *EUVE* data. Dupree et al. have also obtained a minimum for $em(T)$ at $T = 10^{5.8}$ K which however is outside our temperature range.

Following the results of our variability analysis we can assume that the corona of Capella is made of stationary magnetic loops which are the largely dominant (or the only) source of the observed emission. From the physical conditions of the corona of Capella we infer that the pressure is approximately uniform inside these loops, because the pressure scale height, H_p, is of the order of the stellar radius (and much larger than in the solar case), due to the high coronal temperature and to the low surface gravity ($g_* \sim 0.02\, g_\odot$): already for $T = 10^6$ K we obtain $H_p \sim 10^{11}$ cm, which is slightly smaller than the stellar radius ($R_* \sim 10^{12}$ cm), and for $T = 10^7$ K we obtain $H_p \sim 10^{12}$ cm. Therefore we can argue that the pressure has to remain constant along any loop as large as the stellar radius or smaller. As we shall prove in Sect. 4.4, volume estimates based on the analysis of the He-like triplets suggest characteristic lengths ($L \sim 10^9 - 10^{11}$ cm) smaller than the stellar radius, confirming the hypothesis that the plasma in the coronal loops is isobaric.

If we assume the loop model proposed by Rosner et al. (1978), we find that the shape of the emission measure distribution for a single loop does not depend on the size of the loop itself, but only on the loop maximum temperature T_p (Maggio & Peres 1996), and its functional form is $em(T) \propto T^\beta$ for $T < T_p$. We have used the approach proposed by Peres et al. (2001) who show that it is possible to infer information about the coronal structure starting from the consideration that the total $em(T)$ of the whole corona is the sum of the emission measure distributions of individual loops. Under these assumptions Peres et al. have shown that the ascending slope of the $em(T)$ of the whole corona is linked to the β value, and the power-law index $-\alpha$ of the descending slope is linked to the distribution of the maximum temperatures of different classes of coronal loops. We have performed this analysis estimating the ascending and descending slopes of the Capella $em(T)$ in the intervals: $\log T = 6.5 - 6.8$ and $\log T = 6.9 - 7.2$ respectively (Table 5).

Table 5. Ascending and descending slope values for the emission measure distributions. The fitting has been performed over the $\log T$ intervals [6.5,6.8] and [6.9,7.2].

	$em(T)$ Obs. 2000	$em(T)$ Obs. 2001
β	5.7 ± 1.3	6.1 ± 0.9
α	5.7 ± 1.4	5.6 ± 1.1

The value $\beta = 1.5$ corresponds to the hypothesis of constant loop cross-section and uniform heating, and Peres et al. (2001) have shown that the solar $em(T)$ is well described by this model. The much larger values we have found for β (Table 5) suggest two possibilities: 1) the heating is not uniform but higher near the loop footpoints, in this way the temperature profile along the loop is flatter, and therefore the emission measure distribution vs. T is steeper than in the case of uniform heating, since the emission measure is concentrated in a narrower temperature range; 2) the loop cross-section increases with height, implying that there is more emission measure at higher temperatures; it is however hard to get such a steep $em(T)$ even assuming a strong opening. Also the two effects may be both at work, since the two hypothesis are not mutually exclusive.

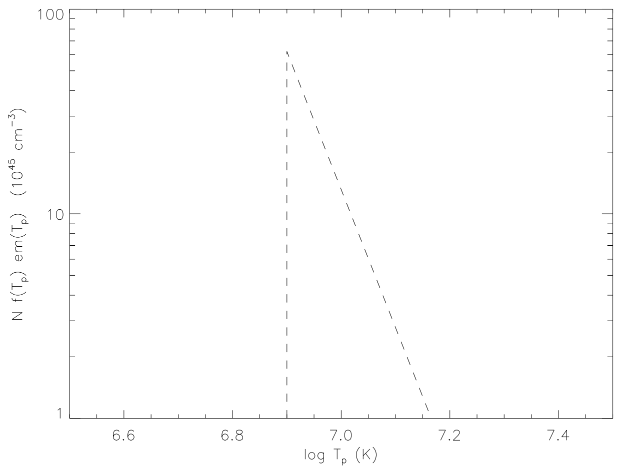

Figure 12. Distribution of loops vs. their maximum temperature T_p.

The high values found for α show that almost all the loops have a T_p value equal to, or only slightly larger than, the peak value of the total emission measure distribution. In Fig. 12 we show the distribution $N\,f(T)\,em(T_p)$ (according to the notation of Peres et al. 2001) of loop maximum temperature, where N is the total number of loops, $f(T)$ is the fraction of loops with maximum temperature T_p, and $em(T_p)$ is the maximum value of the emission measure distribution of one loop with maximum temperature equal to T_p. A consequence of our hypothesis is that the distribution evaluated does not contain a significant amount of loops with maximum temperature lower than the peak temperature $10^{6.8}$ K, however this scenario has to be taken as just an approximation and loops with $T_p < 10^{6.8}$ K may indeed exist albeit having a marginal role in determining the whole corona $em(T)$. We argue that these loops have to exist because the whole $em(T)$ at temperatures smaller than the peak value is not well described by a simple power-law; these loops are responsible for the amount of emission measure observed near $10^{6.3}$ K, but we cannot analyze the $em(T)$ shape near this secondary peak because we have not enough information (in fact we can assign error bars to the emission measure distribution only for $T \geq 10^{6.2}$ K). It is worth noting also that the emission measure distribution obtained by Dupree et al. (2003, Fig. 11) shows a bump near $T = 10^{6.3}$ K, though the amplitude is lower than in our case, confirming our guess about another class of loops with peak temperature of a few million degrees. Moreover, the existence of this loop class will be more evident in the following analysis of the results obtained from the He-like triplets (see Sect. 4.4). Finally we note that we have also marginal indication about a third loop class needed to describe the hottest part of our $em(T)$.

4.3. Density and temperature values from He-like ions

The density values that we have derived are compatible with those obtained by Brinkman et al. (2000), Canizares et al. (2000), Ness et al. (2001), Mewe et al. (2001), Phillips et al. (2001) and Audard et al. (2001). Our results show that the electron density N_e is higher in plasma regions with higher temperature. This finding is also supported by Dupree et al. (1993), they found densities ranging from 10^{11} cm^{-3} to 10^{13} cm^{-3} from the ratios of ultraviolet Fe XXI lines which form at $T \sim 10^7$ K.

As already noted in Sect. 3.4 all the temperature values we have derived from the He-like ions are invariably lower than the corresponding temperature of peak emissivity T_{max}; this finding is puzzling if we consider that, on the basis of the shape of the computed $em(T)$, we would have expected that temperature values estimated from the O VII, Ne IX and Mg XI were higher than the corresponding T_{max} because there is a larger amount of emitting plasma at $T > T_{max}$ than at lower T. As a check we have computed the temperature-sensitive R_T ratios (Sect. 3.4) with line fluxes synthesized from the emission measure distribution and found R_T lower than the observed ones, and the relevant temperature higher than T_{max}.

A possible explanation of this result is that the CHIANTI V3.03 database does not include a sufficient number of dielectronic satellite lines, produced by a doubly excited state in a Li-like ion. If taken into account, these satellite lines yield to higher predicted R_T values, and a higher estimate for T (Porquet et al. 2001). We stress that all the R_T values we have obtained are compatible with those reported by Brinkman et al. (2000), Canizares et al. (2000), Ness et al. (2001), Mewe et al. (2001), Phillips et al. (2001) and Audard et al. (2001), confirming the hypothesis that the observed behavior is linked to the atomic model adopted and not to instrumental effects or line fitting problems.

4.4. Volume and pressure from He-like ions

The values of T and N_e obtained from the study of He-like ions allow us to estimate the effective volume and the average pressure of the region where these lines are formed. To determine the volume V we have evaluated the emission measure $em\,(T^*)$ of the whole region using the resonance line emissivity at the temperature T^* derived from the R_T ratio. Then, the volume is estimated as $V = em\,(T^*)\,/N_e^2$, and the values obtained are shown in Table 6. We stress that this procedure assumes that all the plasma contributing to the He-like emission is concentrated at the single temperature T^*. Phillips et al. (2001) derived from the O VII line triplet an estimate of the volume of $\sim 4\times10^{31}$ cm^3 (with an uncertainty range $1\times10^{31} - 2\times10^{32}$ cm^3), while Behar et al. (2001) have reported a volume of $\sim 10^{29}$ cm^3 at $T = 10^{6.8}$ K, derived from iron lines: both these estimates are consistent with our findings.

In order to derive the size of individual loops from the above estimates of the effective plasma volumes we must consider two effects: each loop is characterized by a large temperature range, while the volumes are based on emission lines which form over a restricted temperature range; moreover the corona of Capella is most likely made of a large number of loops which contribute to the line emission and therefore to the effective volume estimates. We guess that the second effect dominates the first one and therefore the effective volume estimates represent upper limits to individual loop volumes. Hence the characteristic sizes of the coronal structures ($L \sim V^{1/3}$), supported also by the results from Phillips et al. and Behar

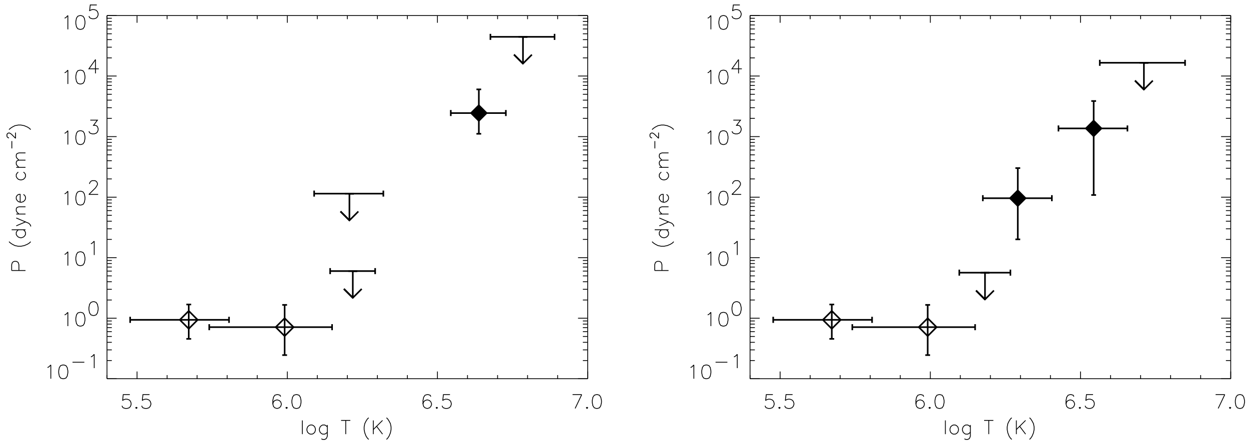

Figure 13. Coronal plasma pressure vs. temperature for the two observations. The pressures are obtained by the density and temperature values evaluated from the analysis of He-like triplets. Filled diamonds and upper limits indicate the values determined by our analysis of O VII, Ne IX, Mg XI and Si XIII triplet, while open diamonds indicate pressures obtained by the C V and N VI analysis made by Ness et al. (2001).

Table 6. Volume of coronal plasma at different temperatures evaluated from density values from He-like triplet diagnostics.

	Obs. 2000			Obs. 2001		
Ion	$\log T^*$	$EM(T^*)\,(cm^{-3})$	$V\,(cm^3)$	$\log T^*$	$EM(T^*)\,(cm^{-3})$	$V\,(cm^3)$
O VII	6.2	$\sim 2 \times 10^{52}$	$> 2 \times 10^{32}$	6.2	$\sim 2 \times 10^{52}$	$> 2 \times 10^{32}$
Ne IX	6.2	$\sim 1 \times 10^{54}$	$> 3 \times 10^{31}$	6.3	$\sim 4 \times 10^{53}$	$\sim 1 \times 10^{31}$
Mg XI	6.6	$\sim 2 \times 10^{53}$	$\sim 5 \times 10^{28}$	6.5	$\sim 4 \times 10^{53}$	$\sim 2 \times 10^{29}$
Si XIII	6.8	$\sim 2 \times 10^{53}$	$> 5 \times 10^{26}$	6.7	$\sim 3 \times 10^{53}$	$> 4 \times 10^{27}$

et al., are $\sim 10^{11}$ cm for plasma at $T \sim 10^6$ K and $\sim 10^9$ cm for $T \sim 10^7$ K. The comparison between these characteristic lengths and the pressure scale height confirms the hypothesis of isobaric loops.

We have noted above (Sect. 3.4) that the temperatures T^* derived from the observed R_T may be slightly underestimated, implying that the volumes obtained using these temperatures may be imprecise. To quantify this effect we have also evaluated the volume values using, instead of T^*, the effective temperatures obtained from the R_T ratio evaluated by the predicted line fluxes: the volumes obtained are smaller by a factor $2-5$, and therefore the hypothesis of constant pressure loops are even more confirmed.

As a further step it is possible to estimate the average pressure P, relative to the region where the triplets are formed, from the value of T^* and N_e. In Fig. 13 we show plots of P vs. T^* for the two observations. From this plot we deduce that the plasma present in the corona of Capella, confined in magnetic loops, is characterized by very different pressure values: in particular, we have found that regions the higher temperature the larger the pressure values. We note that this result is not in conflict with the hypothesis of constant pressure loops: in fact, it may happen that the pressure is very different from one loop to another, but remains constant inside each loop. We can state that different loop classes with different pressures characterize the corona of Capella, and loops with higher pressures have also higher values of maximum temperature T_p. Recalling the shape of the emission measure distribution (Fig. 11) and the analysis made in Sect. 4.2, we can tentatively identify the high-pressure loops with the dominant class of coronal structures having $T_p \sim 10^{6.8}$ K, and the low-pressure loops with the structures determining the secondary peak in the $em(T)$ at $T \sim 10^{6.3}$ K. In order to test qualitatively this coronal model, we plan to perform detailed simulations, whose results will be reported in a subsequent paper.

5. Conclusions

In this work we have analyzed two LETGS observations of Capella for which we have identified and measured the strongest emission lines. Starting from the reconstructed emission measure distribution we have obtained information about the structure of individual loops and we have derived the coronal loop distribution vs. peak temperature. The corona of Capella appears to be composed mainly of stable coronal structures in isobaric conditions, with characteristic sizes most likely smaller than the stellar radius, but such structures appear to have plasma emission measure distributions vs. temperature steeper than in the case of solar-like coronal structures. Our analysis indicates that different loop classes are needed to describe the corona of Capella: the dominant class is composed of loops having peak temperatures $T_P \sim 10^{6.8}$ K, but we have also found evidence of at least another class of loops having $T_P \leq 10^{6.3}$ K. In fact, the average pressure, estimated from the analysis of the He-like triplets, is significantly lower at $T \leq 1.5 \times 10^6$ K than at higher temperatures: since the loops are isobaric, this result indicates that the hotter loops must have plasma pressure higher than cooler loops.

Ayres et al. (1998), studying the broadening of UV lines with $T_{\max} \sim 10^{4.5} - 10^{5.5}$ K in the Capella spectra taken with the Goddard High-Resolution Spectrometer of the *Hubble Space Telescope*, have suggested the existence of transition zone structures, having sizes comparable to the stellar radius, in which the plasma pressure, evaluated from the density-sensitive O IV line ratios, is $P \sim 0.2$ dyne cm^{-2} at $T \sim 10^{5.2}$ K (Linsky et al. 1995). This value is compatible with the pressure estimated at $T \sim 10^6$ K within statistical uncertainties. However we argue that if these structures are the footpoints of the cool coronal loops, it is difficult to reconcile their extent with the hypothesis of isobaricity. On the other hand, the structures evidenced by Ayres et al. are certainly not in pressure equilibrium with the coronal loops which explain the bulk of the X-ray (and EUV) emission from Capella.

The next step in our investigation will be to derive a more detailed model of the corona which will help us to interpret all the observational evidences presented in this paper.

Acknowledgements. We thank V. Kashyap and J. Drake for allowing us to use their software for the emission measure reconstruction. We also thank J. Sanz-Forcada who provided us with the emission measure distribution of Capella derived from a recent *EUVE* observation. Finally we acknowledge partial support for this work by Agenzia Spaziale Italiana and Ministero dell'Istruzione, dell'Università e della Ricerca.

Appendix A: Line identifications

In this section we report some notes about our line list, based upon the CHIANTI V3.03 database, and about the comparison with previously published line lists derived from other Capella X-ray observations.

The spectral region between 10 and 12 Å (Fig. A.1) contains many weak spectral features whose identifications is not straightforward. The most relevant differences between our list and those of Phillips et al. (2001) and Behar et al. (2001) are restricted to this spectral range, where, like Ayres et al. (2001), we have identified lines from iron with ionization levels higher than what reported by Phillips et al. and Behar et al.

10.66 Å We have identified this spectral feature as an unresolved blend of the Fe XXIV $1s^2\,3p \rightarrow 1s^2\,2s$ doublet, the same choice has been done by Ayres et al., while Phillips et al. have ascribed it to the Fe XIX $2p^3\,4d\ ^3P_2 \rightarrow 2p^4\ ^3P_1$ 10.644 Å transition which is not in CHIANTI. None of these identifications is present in Behar et al.

11.02 Å We have ascribed this feature to a blend of Fe XVII $2s\,2p^6\,4p \rightarrow 2s^2\,2p^6$ 11.023 Å, Fe XXIII $2s\,3p \rightarrow 2s^2$ 10.981, 11.018 Å, and Fe XXIV $1s^2\,3d \rightarrow 1s^2\,2p$ 11.029 Å lines, Ayres et al. report only the Fe XXIII and Fe XXIV contributions. Instead, Behar et al. and Phillips et al. have reported a blend between the same Fe XVII line above and the Ne IX $1s\,4p \rightarrow 1s^2$ 11.009 Å line. The latter transition is present in CHIANTI, but its predicted intensity is negligible with respect to the other contributions.

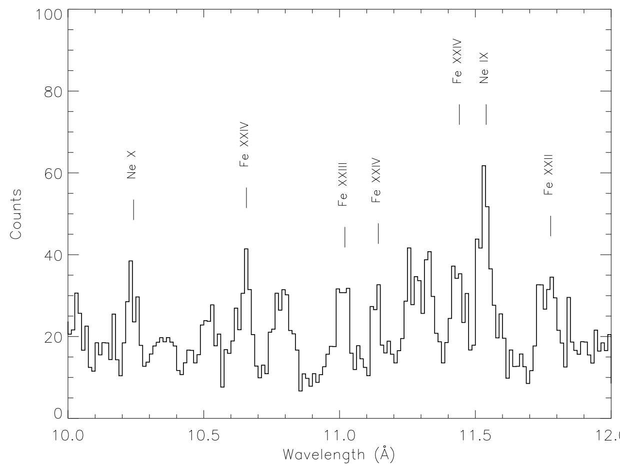

Figure A.1. LETGS spectrum of Capella (observation taken in 2000, positive and negative orders added) in the region 10 – 12 Å.

11.14 Å We have identified this feature with the Fe XXIV $1s^2\,3d \rightarrow 1s^2\,3p$ 11.171 Å line. Phillips et al. and Ayres et al. have made the same identification but included also a (resolved) contribution from the Fe XVII $2p^5\,5d\ ^1P_1 \rightarrow 2p^6\ ^1S_0$ 11.129 Å transition[5], which is not available in the CHIANTI database. The Fe XVII transition is the only one identified by Behar et al.

11.44 Å We have identified this spectral feature as a blend between Fe XXII and Fe XXIV, Ayres et al. indicate only the contribution of Fe XXII, while Behar et al. and Phillips et al. have reported a Fe XVIII $2p^4\,4d\ ^4P_{5/2} \rightarrow 2p^5\ ^2P_{3/2}$ 11.420 Å line which is not included in the CHIANTI database.

Brown et al. (2002), using EBIT measures, have shown that the intensity of Fe XXIV lines at 11.02 and 11.44 Å are respectively 0.6 and 0.4 times the intensity of the Fe XXIV line at 11.17 Å[6]. From these results we deduce that, since the line at 11.17 Å is detected, as Phillips et al. do, the other two transitions have to be of the same order of magnitude, and this conclusion supports our identifications. Moreover, the CHIANTI database contains the Fe XVII and Ne IX lines at 11.02 Å, included by Phillips et al. and Behar et al. in their line lists, but the CHIANTI predicted intensities of the Fe XXIII and Fe XXIV lines at 11.02 Å are much higher and hence they dominate the blends.

It is worth noting that the identifications we have made of these highly-ionized iron lines turn out to be very important to constrain the high temperature tail of the emission measure distribution, as illustrated in Sect. 3.2, and more in de-

[5] The measured fluxes reported by Phillips et al. indicate that the Fe XXIV intensity is 0.5 times the Fe XVII one, therefore our measured fluxes ascribed to the Fe XXIV possibly is slightly overestimated. We note however that our measured line flux results compatible with the other Fe XXIV lines, and so, as reported in Appendix B, we use also this line in the emission measure reconstruction.

[6] Brown et al. do not measure the intensity of the Fe XXIV line at 10.66 Å because it is out of wavelength range they have explored.

tail in Appendix B. Finally we also note that in this region other spectral features are present (mainly at 10.5, 10.8 and 11.3 Å) but no predicted lines in the CHIANTI database are available to identify them. Some of these features are identified by Phillips et al. (Fe XIX $2p^3\,4d\,(^2P)\,^3D_2 \rightarrow 2p^4\;^3P_1$ at 10.644 Å, $2p^3\,4d\,(^2D)\,^3D_2 \rightarrow 2p^4\;^3P_1$ at 10.770 Å and $2p^3\,4d\,(^4S)\,^3D_3 \rightarrow 2p^4\;^3P_2$ at 10.813 Å, Fe XVII $2p^5\,5d\;^3D_1 \rightarrow 2p^6\;^1S_0$ at 11.250 Å, and Fe XVIII $2p^4\,4d\;^2F,\;^2D,\;^2P \rightarrow 2p^5\;^2P_{3/2}$ at 11.326 Å), and by Behar et al. (with the only difference of the Fe XVII $2p^5\,6d \rightarrow 2p^6$ at 10.782 Å instead of the Fe XIX line) with transitions from highly excited ($n > 4$) states.

From all the above considerations, we note that the spectral features at 10.66, 11.14 and 11.44 Å should contain also contributions from Fe XVII-Fe XIX lines not included in the CHIANTI database, therefore we may have slightly overestimated the line counts ascribed to Fe XXII-Fe XXIV lines. In order to quantify this effect we have evaluated the predicted line intensities at 10.66, 11.14 and 11.44 Å with the help of the Astrophysical Plasma Emission Database (as implemented in the ATOMDB V1.3), and found that the lines we have identified are responsible for about 30-40% of the total intensities in the observed spectral features. In the light of this result we have performed a trial reconstruction of the emission measure distribution taking into account these corrections to the measured fluxes of the above three lines: we have verified that for $\log T < 7.2$ the new $em(T)$ is virtually the same as the one reported in Sect. 3.2 (Fig. 2), while for $\log T \geq 7.2$ it results lower by a factor ~ 2, but anyway compatible with it within the statistical uncertainties.

Appendix B: Line selection for $em(T)$ reconstruction

We report a commented list of the lines selected (or excluded) for the reconstruction of the emission measure distribution with the MCMC method[7], sorted by element and, for iron lines only, by ionization stage.

Fe IX The line at 171.07 Å has been included in the subset. We guess that also this line may be influenced by the bias which affects other lines at $\lambda > 80$ Å lines (see Sect. 3.2); nonetheless we have retained this line because it is useful to constrain the amount of emission measure at low temperature: in fact this is the line with the lowest $T_{\rm max}$ we have measured.

Fe XVI Lines at 54.13, 54.71, 66.25 and 66.36 Å agree with each other, and so they have been included[8], while the line at 63.71 Å has been ruled out because its flux is too small in both observations.

Fe XVII From the whole set of Fe XVII lines we have rejected only those at 13.89 and 16.34 Å, because they would require an emission measure at their $T_{\rm max}$ higher than suggested by the other Fe XVII lines.

Fe XVIII Many of the Fe XVIII lines are affected by severe blending effects, which may cause the large spread in the emission measure values inferred from the line fluxes. We have found an acceptable agreement among the lines at 13.95, 14.26, 14.37, 14.53, 15.45, 16.07 and 16.31 Å. The line at 15.83 Å has been included in our subset only for the analysis of the March 2000 spectrum, in fact the measured line counts for the observation taken in 2001 result too high. We have rejected strong lines at 14.22, 16.17, 17.64, 93.92 and 103.94 Å because they require emission measure values too small in comparison with other Fe XVII lines. Opposite behavior is shown by the line at 15.62 Å. Finally the line at 15.87 Å has a contribution function $G(T)$ too low to explain the measured flux, so we are not sure of its identification; in the CHIANTI database however no other sufficiently strong line is present at this wavelength.

Fe XIX The lines at 13.52 and 13.80 Å, though blended with the Ne IX triplet, have been selected, while the line at 13.67 Å has been included only in the subset for March 2000 observation, because the line counts in the 2001 observation is too high. We have excluded the line at 13.57 Å because it contains the density-sensitive intercombination line of the Ne IX triplet, though it agrees with other Fe XIX lines. As done for other iron ions we have rejected long wavelength lines (91.01, 101.55, 108.36 and 119.98 Å) since they provide too small emission measure values.

Fe XX We have only retained the strong line at 12.82 Å, which is compatible with other iron lines. The line at 13.74 Å has been rejected because the emission measure required is too high. We have excluded also the lines at 118.68, 121.84 and 132.84 Å because of the bias which affects the spectral features at long wavelength (Sect. 3.2).

Fe XXI The line at 12.28 Å requires an emission measure larger than that appropriated for the 128.75 Å line; we have included only the first one in the subset because we consider more reliable the lines at short wavelengths (Sect. 3.2).

Fe XXII The line at 11.77 Å, though it has low signal to noise ratio, agrees with other iron lines, and so we have included it in the subset. The line at 117.18 Å has a contribution function too small to explain the measured flux, casting doubts on its identification (but there is no alternative in the CHIANTI database). Finally we have rejected the line at 135.76 Å because its flux is too small for the emission measure determined from our analysis.

Fe XXIII We have selected the line at 11.02 Å, while the one at 132.91 Å has been excluded because of the problem affecting the lines at long wavelengths (Sect. 3.2).

[7] Each spectral feature, which has been identified with more than one atomic transition, is referred to the ion responsible for the major contribution.

[8] We note however that the total counts in the lines at 66.25 and 66.36 Å may have been slightly overestimated because of the presence of the O VII line at 22.10 Å at the third order.

Fe XXIV The lines at 10.62, 11.17 and 11.43 Å agree quite well among themselves, therefore we have taken into account all of them.

C The C VI lines at 26.99 and 28.47 Å have few line counts to be considered reliable, so we have selected only the C VI line at 33.73 Å.

N The N VII line at 24.78 Å and the N VI line at 28.79 Å show a general agreement among themselves, and so we have included them in the subset. We have ruled out the forbidden line of the N VI He-like triplet at 29.53 Å because it is density-sensitive.

O We have selected the O VIII lines at 18.63, 18.97 Å and the O VII resonance line at 21.60 Å. The O VIII lines at 15.18 and 16.01 Å have been excluded because they require emission measure values too high in comparison with those provided by other oxygen lines. We have excluded the intercombination and forbidden lines of the O VII He-like triplet because they are density-sensitive.

Ne The identified neon lines do not show agreement among themselves, probably because too weak (the Ne X at 10.24 Å) or strongly blended with iron lines (in the case of the Ne IX triplet); therefore we have retained only the strongest one, that is to say the Ne X L_α line at 12.13 Å.

Mg We have selected the Mg XII line at 8.42 Å, the Mg XI line at 9.17 Å and the Mg X lines at 57.88 and 57.92 Å, while we have excluded the intercombination and forbidden lines of the Mg XI He-like triplet.

Si Among the whole set of silicon lines identified, which are the Si X line at 50.52 and 50.69 Å, the Si XI line at 49.22 Å, the Si XII line at 44.02, 44.17, 45.52 and 45.59 Å, the Si XIII triplet and the Si XIV line at 6.18 Å, we have excluded only the intercombination and forbidden lines of the Si XIII He-like triplet because they are density-sensitive.

Ni All the Ni XIX line identified, whose wavelengths are 12.44, 14.04 and 14.08 Å, agree with each other and so they have been selected.

We have considered several effects which may cause the disagreement between the observed intensities of iron lines ascribed to the same ionization stage but falling at short and long wavelengths. In particular we have analyzed effects due to uncertainties in the effective area, interstellar hydrogen column density higher than assumed and excess background subtraction. We have found that none of these effects by itself can to explain the discrepancy we observe. A further possibility to be investigated may be related to the data reduction procedure. Note however that in the short wavelength region ($\lambda < 80$ Å) we have identified and measured a sufficient number of strong lines which sample adequately temperatures ranging from $10^{6.1}$ K to $10^{7.3}$ K, therefore our emission measure reconstruction is not affected significantly by having neglected the few Fe XVIII-Fe XXIII lines at long wavelengths.

References

Audard, M., Behar, E., Güdel, M., et al. 2001, A&A, 365, L329
Ayres, T. R., Brown, A., Osten, R. A., et al. 2001, ApJ, 549, 554
Ayres, T. R., Simon, T., Stern, R. A., et al. 1998, ApJ, 496, 428
Bauer, F. & Bregman, J. N. 1996, ApJ, 457, 382
Behar, E., Cottam, J., & Kahn, S. M. 2001, ApJ, 548, 966
Brickhouse, N. S., Dupree, A. K., Edgar, R. J., et al. 2000, ApJ, 530, 387
Brinkman, A. C., Gunsing, C. J. T., Kaastra, J. S., et al. 2000, ApJ, 530, L111
Brown, G. V., Beiersdorfer, P., Liedahl, D. A., et al. 2002, ApJS, 140, 589
Canizares, C. R., Huenemoerder, D. P., Davis, D. S., et al. 2000, ApJ, 539, L41
Collura, A., Maggio, A., Sciortino, S., et al. 1987, ApJ, 315, 340
Dupree, A. K., Brickhouse, N. S., Doschek, G. A., Green, J. C., & Raymond, J. C. 1993, ApJ, 418, L41
Dupree, A. K., Brickhouse, N. S., & Sanz-Forcada, J. 1999, Bulletin of the American Astronomical Society, 31, 1483
—. 2003, In preparation
Favata, F., Mewe, R., Brickhouse, N. S., et al. 1997, A&A, 324, L37
Gabriel, A. H. & Jordan, C. 1969, MNRAS, 145, 241
Grevesse, N., Noels, A., & Sauval, A. J. 1992, in Coronal Streamers, Coronal Loops, and Coronal and Solar Wind Composition, 305–308
Hummel, C. A., Armstrong, J. T., Quirrenbach, A., et al. 1994, AJ, 107, 1859
Johnson, O., Drake, J. J., Kashyap, V., et al. 2002, ApJ, 565, L97
Kashyap, V. & Drake, J. J. 1998, ApJ, 503, 450
Kashyap, V. L. & Drake, J. J. 2000, AAS/High Energy Astrophysics Division
Keenan, F. P., Kingston, A. E., & Tayal, S. S. 1984, Sol. Phys., 92, 75
Linsky, J. L., Brown, A., Gayley, K., et al. 1993, ApJ, 402, 694
Linsky, J. L., Wood, B. E., Brown, A., & Osten, R. A. 1998, ApJ, 492, 767
Linsky, J. L., Wood, B. E., Judge, P., et al. 1995, ApJ, 442, 381
Maggio, A. & Peres, G. 1996, A&A, 306, 563
Mazzotta, P., Mazzitelli, G., Colafrancesco, S., & Vittorio, N. 1998, A&AS, 133, 403
Mewe, R., Raassen, A. J. J., Drake, J. J., et al. 2001, A&A, 368, 888
Ness, J.-U., Mewe, R., Schmitt, J. H. M. M., et al. 2001, A&A, 367, 282
Ness, J.-U., Schmitt, J. H. M. M., Burwitz, V., et al. 2002, A&A, 394, 911
Peres, G., Orlando, S., Reale, F., & Rosner, R. 2001, ApJ, 563, 1045
Perryman, M. A. C., Lindegren, L., Kovalevsky, J., et al. 1997, A&A, 323, L49
Phillips, K. J. H., Mathioudakis, M., Huenemoerder, D. P., et al. 2001, MNRAS, 325, 1500
Porquet, D. & Dubau, J. 2000, A&AS, 143, 495

Porquet, D., Mewe, R., Dubau, J., Raassen, A. J. J., & Kaastra, J. S. 2001, A&A, 376, 1113
Pradhan, A. K. 1982, ApJ, 263, 477
Rosner, R., Tucker, W. H., & Vaiana, G. S. 1978, ApJ, 220, 643
Schrijver, C. J., Mewe, R., van den Oord, G. H. J., & Kaastra, J. S. 1995, A&A, 302, 438
Young, P. R., Dupree, A. K., Wood, B. E., et al. 2001, ApJ, 555, L121